

Visualization and Image Based Characterization of
Hydrodynamic Cavity Bubbles for Kidney Stone
Treatment

by

Dođan Üzüřen

Submitted to the Graduate School of Sabancı University
in partial fulfilment of the requirements for the degree of
Master of Science

Sabancı University

August 2014

Visualization and Image Based Characterization of Hydrodynamic Cavity

Bubbles for Kidney Stone Treatment

APPROVED BY:

Prof. Dr. Mustafa Ünel
(Thesis Advisor)



Assoc. Prof. Dr. Ali Koşar



Assist. Prof. Dr. Hüseyin Üvet



DATE OF APPROVAL:



© Dođan Üzüſen 2014

All Rights Reserved

Visualization and Image Based Characterization of Hydrodynamic Cavity Bubbles for Kidney Stone Treatment

Doğan Üzüşen

ME, Master's Thesis, 2014

Thesis Supervisor: Prof. Dr. Mustafa Ünel

Keywords: Microscopic Images, PIV, Visualization, Median Filter, Morphological Filters, Image Segmentation, Micro-fluidics, Bubble Detection, Tracking

Abstract

Accurate detection, tracking and classification of micro structures through high speed imaging are very important in many biomedical applications. In particular, visualization and characterization of hydrodynamic cavity bubbles in breaking kidney stones have become a real challenge for researchers. Various micro imaging techniques have been used to monitor either an entire bubble cloud or individual bubbles within the cloud.

The main target of this thesis is to perform an image based characterization of hydrodynamic cavity bubbles for kidney stone treatment by designing and constructing a new imaging setup and implementing several image processing and computer vision algorithms for detecting, tracking and classifying cavity bubbles. A high speed CMOS camera with a long distance microscope illuminated by 2 pulsed 198 high performance LED arrays is designed. This system and a μ -PIV setup are used for capturing images of high speed bubbles. Several image processing algorithms including median and morphological filters, segmentation, edge detection and contour extraction algorithms are extensively used for the detection of the bubbles. Furthermore, incremental self-tuning particle filtering (ISPF) method is utilized to track the motion of the high speed cavity bubbles. These bubbles are also classified by their geometric features such as size, shape and orientation. An extensive visualisation work is conducted on the new setup and cavity bubbles are successfully detected, tracked and classified from the microscopic images. Despite very low exposure times and high speed motion of the bubbles, developed system and methods work in a very robust manner. All the algorithms are implemented in Microsoft Visual C++ using OpenCV 2.4.2 library.

Böbrek Taşı Tedavisi için Hidrodinamik Kavite Kabarcıklarının Görüntülenmesi ve Görüntü Tabanlı Karakterizasyonu

Dođan Üzüşen

ME, Master Tezi, 2014

Tez Danışmanı: Prof. Dr. Mustafa Ünel

Anahtar Kelimeler: Mikroskopik Görüntüler, PIV, Görüntüleme, Medyan Filtre, Morfolojik Filtreler, Görüntü Bölütleme, Mikro-akışkanlar, Kabarcık Tespiti, Takip

Özet

Birçok biyomedikal uygulamalarda doğru şekilde tesbit, izleme ve yüksek hızda görüntüleme yoluyla mikro yapıların sınıflandırılması çok önemlidir. Özellikle, böbrek taşlarının parçalanmasında kullanılan hidrodinamik kavite kabarcıklarının görüntülenmesi ve karakterizasyonu araştırmacılar için gerçek bir sorun haline gelmiştir. Çeşitli mikro görüntüleme teknikleri hem bütün bir kabarcık bulutunu hem de bulut içinde bulunan kabarcıkları tek tek izlemek için kullanılmıştır.

Bu tezin ana hedefi yeni bir görüntüleme düzeneđi tasarlayıp, inşa ederek kavite kabarcıklarının tespiti, takibi ve sınıflandırması adına çeşitli görüntü işleme ve bilgisayar ile görme algoritmaları yardımıyla böbrek taşı tedavisi için hidrodinamik kavite kabarcıklarının görüntü tabanlı karakterizasyonunu yapmaktır. 2 adet darbeli 198 yüksek performanslı LED tarafından aydınlatılan yüksek hızlı bir CMOS kamera ile bir uzun mesafe mikroskop tasarlanmıştır. Bu sistem ve μ -PIV kurulumu yüksek hızlı kabarcıkların görüntülerini yakalamak için kullanılmıştır. Medyan ve morfolojik filtreler, bölütleme, kenar bulma ve kontur çıkarma algoritmaları dahil olmak üzere birçok görüntü işleme algoritması kabarcıkların tespiti için yoğun bir şekilde kullanılmıştır. Ayrıca, artarak kendini ayarlayan parçacık filtre (ISPF) yöntemi yüksek hızlı kavite kabarcıklarının hareketini izlemek için kullanılmıştır. Bu kabarcıklar aynı zamanda boyut, şekil ve yön gibi geometrik özelliklere göre sınıflandırılmıştır. Yeni kurulum üzerinde kapsamlı bir görüntüleme işlemi gerçekleştirilmiş ve mikroskopik görüntülerden kavite kabarcıklarının tespiti, takibi ve sınıflandırılması başarıyla gerçekleştirilmiştir. Geliştirilen sistem ve yöntemler, çok düşük pozlandırma sürelerine ve kabarcıkların yüksek hızlı hareketine rağmen oldukça dayanıklı bir şekilde çalışmaktadır. Tüm algoritmalar Microsoft Visual C++ ve OpenCV 2.4.2 kütüphaneleri kullanılarak gerçekleştirilmiştir.

Acknowledgements

Foremost, I would like to express my sincere gratitude to my supervisor Prof. Dr. Mustafa Ünel for his continuous support patience, motivation, enthusiasm, and immense knowledge. He took me beyond the boundaries of exploring attractive subjects. He was especially positive and spent some of his most valuable time for helping me regarding all my problems. He was always instrumental in opening the locked doors. I could not have dreamed having a better advisor and life mentor.

I would also like to state my appreciation to each of my thesis jury members, Assoc. Prof. Ali Koşar and Assist. Prof. Hüseyin Üvet for their valuable feedback. Throughout my M.Sc. studies, Prof. Koşar always encouraged and supported me to improve myself further. I appreciate his enthusiasm and motivation. It was also an honour for me to work with Assist. Prof. Hüseyin Üvet in the same project.

I would like to acknowledge the support provided by TÜBİTAK through the project 113S092 (Hidrodinamik Kaviteyona Dayanan Medikal Uygulamalar için Kullanılacak Ulusal Endoskopik Cihaz Tasarımı ve Geliştirilmesi) where I had a chance to work with a group of talented people in an exciting environment.

I am deeply grateful to my beloved parents, Fatoş Üzüşen and Seyfettin Üzüşen for their invaluable love, caring and support throughout my life.

I would like to thank to my precious brother Hakan Üzüşen for everything and I will always motivate and support him throughout my life.

Finally, I would like to thank Ayşe Nilay Er for her encouragement and never ending support through my graduate education.

Contents

- 1. **Introduction** **1**
 - 1.1. Objective..... 5
 - 1.2. Structure of the Thesis and Contributions..... 6

- 2. **Background** **8**
 - 2.1. Visualization Techniques..... 8
 - 2.1.1. Particle Image Velocimetry 8
 - 2.1.2. Particle Shadow Sizer 13
 - 2.1.3. Phase Doppler Anemometry 13
 - 2.1.4. Interferometric Particle Imaging 15
 - 2.2. Image Processing Techniques 17
 - 2.2.1. Image Segmentation 18
 - 2.2.1.1. Segmentation Based on Detection 18
 - 2.2.1.2. Thresholding Method..... 18
 - 2.2.1.3. Region Based on Detection 19
 - 2.2.1.4. Segmentation Methods Based on PDE 19
 - 2.2.2. Morphology 20
 - 2.3. Object Tracking Techniques..... 21
 - 2.4. Cavitation Techniques..... 21

| | |
|--|-----------|
| 2.4.1. Hydrodynamic Cavitation | 21 |
| 2.4.2. Ultrasound Cavitation | 23 |
| 3. Quantification of Cavity Bubbles Using a High Speed Camera System with LED Based Illumination..... | 25 |
| 3.1. Visualization System and Image Acquisition..... | 25 |
| 3.2. Image Processing of Microscale Bubbly Cavitation | 27 |
| 3.2.1. Background Noise Removal..... | 27 |
| 3.2.2. Image Enhancement..... | 27 |
| 3.2.3. Morphological Image Processing | 28 |
| 3.2.4. Extracting Bubble Properties..... | 29 |
| 3.2.4.1. Bubble Detection..... | 29 |
| 3.2.4.2. Bubble Size Estimation..... | 31 |
| 3.3. Bubble Tracking..... | 33 |
| 3.2. Hydrodynamic Cavitation Experimental Setup Optimization | 35 |
| 4. Experimental and Image Analysis Results | 37 |
| 4.1. Experimental Results..... | 37 |
| 4.1.1. Experimental Setup | 37 |
| 4.1.2. Results for Image Acquisition | 39 |
| 4.1.3. Results for Image Processing and Characterization of Cavity Bubbles | 40 |
| 5. Conclusion and Future Works | 50 |
| REFERENCES | 52 |

List of Figures

| | | |
|------|---|----|
| 1.1 | Micro fluids Visualization Solutions: (a) Particle Image Velocimetry (PIV), (b) Phase Doppler Anemometry (PDA), (c) Inteferometric Particle Imaging (IPI), (d) Micro Particle Shadow Sizer, (e) Back illumination Setup, (f) Micro Strobe | 4 |
| 2.1 | Particle Image Velocimetry (PIV) Configuration [72] | 9 |
| 2.2 | Particle Image Velocimetry (PIV) Principle [72] | 10 |
| 2.3 | Particle Shadow Sizer (PSS) Configuration [72]..... | 13 |
| 2.4 | Phase Doppler Anemometry (PDA) Configuration [72] | 15 |
| 2.5 | Generation of the two Glare points by a transparent particle [72] | 16 |
| 2.6 | IPI Optical Configuration, Φ is the scattering angle or observation angle..... | 17 |
| 2.7 | (a) Microchannel configuration with the orifice throat and exit area and experimental placement of the kidney stone (b) Experimental setup..... | 23 |
| 3.1 | (a) Original image, (b) Image after histogram equalization | 28 |
| 3.2 | Segmentation of planar bubble image around a working point..... | 31 |
| 3.3 | Oblate spheroid with main axes (major axes <i>A</i> and <i>C</i> , minor axis <i>B</i>)..... | 32 |
| 3.4 | Example of subspace learned by the IPCA method | 34 |
| 3.5 | Comparison of experimental erosion rate with predictions of the proposed correlation | 36 |
| 4.1 | Experimental Setup..... | 38 |
| 4.2 | Bubble cloud emerging from the probe exit at different cavitation intensities | 39 |
| 4.3 | Bubble cloud emerging that is captured through increasing distance from the probe exit, respectively | 40 |
| 4.4 | Original flow image | 40 |
| 4.5 | Deblurred flow image | 41 |
| 4.6 | Flow image filtered for background noise removal | 42 |
| 4.7 | The enhanced flow Image | 43 |
| 4.8 | The morphological filled cavity bubble shape | 44 |
| 4.9 | The recognized edges of cavity bubbles | 45 |
| 4.10 | Results of the processing operations of high speed cavity bubbles micro-flow images | 45 |
| 4.11 | Pseudo-colour indexed image..... | 46 |

| | | |
|------|---|----|
| 4.12 | Schematic diagram of the filter operations for phase discrimination by extracting the images of tracer particles from the pictures of the Hydrodynamic cavitation flow..... | 47 |
| 4.13 | (a) Original μ PIV Image (b) Filtered only tracer partial Image (c) Velocity vector map of the hydrodynamic cavitation (d) Instantaneous flow field of the continuous phase in the bubble column overlapped onto the original image containing bubbles and tracer. Mean velocities of the vector field have been subtracted to visualize the fluctuations (the colours of the vectors indicate the fluid velocity magnitude. Red: high velocity, blue: low velocity)..... | 48 |
| 4.14 | Cavity bubbles tracking results of the ISPF algorithm..... | 49 |

List of Tables

4.1 Detection and classification of individual bubbles..... 46

Chapter I

1 Introduction

With the recent advances in micro/nano technology, various sophisticated microfluidic devices such as micro-bioreactors, micro-heat exchangers, μ -TAS (total analysis system), Lab-on-a-chip (LOC) and fluidic logic devices have been applied widely in the field of biomedical and process engineering [1-3]. These kinds of microfluidic devices, particularly bio-chips, have different types of microchannels. The Reynolds numbers for microchannels are generally quite low and the character of the flow at microscale is typically laminar. However, numerical flow simulations are difficult to accomplish because of complex fluid characteristics and flow geometries, surface phenomena such as field gradients, fluid-structure interaction, etc. The exhaustive analysis and the reliable experimental characterization of the 2D/3D flow inside the micro channels play a key role in their proper and effective design and the confirmation of numerical flow simulations. In order to analyze the flow phenomena in microfluidics, a convenient experimental technique that can solve the volatile and spatial resolutions of the given micro-flow is definitely needed [4-5].

For a comprehensive analysis of two-phase flows, uninterrupted optical techniques are most proper. This type of measurement techniques should provide the velocity fields of both phases and the local particle size distributions throughout the conceived two-phase system. Particle image velocimetry (PIV) is a technique that is applied by Santiago et al. [6] for the first time in order to measure flow fields in microfluidic systems due to its capability to measure whole field, sudden fluid motion. In a typical PIV, a thin sheet of laser light is generated from pulse laser for illumination of a single plane within the fluid flow, hence determining the measurement region of the PIV system. In micro-PIV (μ PIV) which is shown

in Figure 1.1 (a), laser sheet generation is not practicable, and the entire volume of the flow is illuminated and now the depth of focus of the microscope objective determines the measurement section. Because the experimental environment in μ PIV is quite distinct to larger scale type of PIV, a separate research and definition of LED illumination for μ PIV applications can be performed. There are a few previous micro-PIV studies where LEDs have been used as illumination sources [7-8]. Rather than a typical PIV laser system, a LED illumination system has many advantages such as small size, adaptability to different range of wavelengths, freely tuning pulse length and repetition rate, low energy requirement and very low cost. One of the main disadvantages is the lower light intensity. This problem can be solved by regulations in the setup, as will be described in more detail in the next sections. Image acquisition, that is record of an image in digital form, is absolutely the first step in any image processing system. Particle images of fluid motion are captured by double exposure mode CMOS camera; two sequential particle images distinguished by specified time interval between two laser pulses are captured. One of the main reasons why high-speed CMOS cameras are used for recording purpose of microfluids is high resolution property under various conditions; thus acquired data from images can be directly processed with the existing computer vision techniques for extracting and tracking objects. Hydrodynamic cavitation is the generation of vapour bubbles due to the sudden drop in pressure when a liquid flows through a constriction [25-27] and limiting only to bubbly flows, the application of phase-Doppler anemometry (PDA) is not fully satisfying since bubbles are only spherical up to a diameter of about 1.0 mm and thus larger bubbles which are most pertinent for technical operations cannot be measured correctly [9-10]. In recent years, methods of pulse-light velocimetry (PLV), such as PIV and particle tracking velocimetry (PTV) have been applied to bubbly flows [11-21]. Crucial for a robust and

simultaneous velocity measurement of both phases (i.e. liquid and bubbles) is the separation of images comprised of tracer particles and bubbles.

Monitoring microscopic images and processing them using several robust vision modules in the context of micro-manipulation were carried out in the past [22-24]. In particular, visualization and characterization of cavity bubbles in breaking kidney stones have become a real challenge for researchers. Various micro imaging techniques have been used to monitor either an entire bubble cloud or individual bubbles within the cloud, where the shape of the bubbles is also essential so image segmentation is a significant task in robust image analysis and a principle process of low-level vision which provide important data for further image processing. In many image analysis applications, it is generally the first, most fundamental and most difficult step. Also outputs of the computer vision algorithms simplify the solution of many difficulties such as low illumination, out of focus etc. This fact is one of the main motivations for applying image processing techniques.

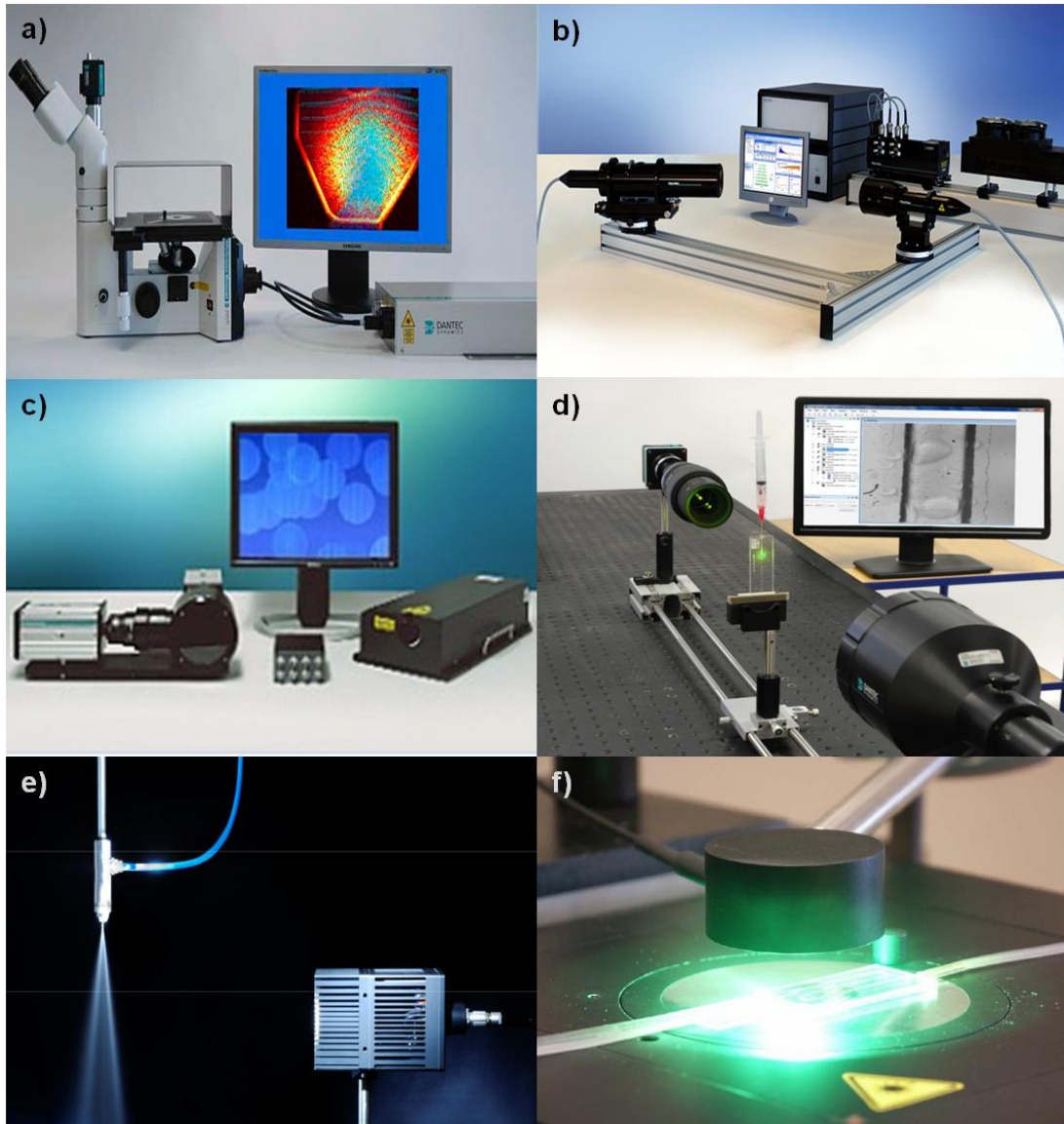


Figure 1.1 : Micro fluids Visualization Solutions: (a) Particle Image Velocimetry (PIV), (b) Phase Doppler Anemometry (PDA), (c) Interferometric Particle Imaging (IPI), (d) Micro Particle Shadow Sizer, (e) Back illumination Setup, (f) Micro Strobe

1.1 Objective

The main target of this thesis is to perform visualization and an image based characterization of micro-scale hydrodynamic bubbly cavitation and utilizes image analysis algorithms for capturing, extracting and classifying cavitation bubbles that are used in kidney stone treatment. An extensive visualisation work is conducted using a high resolution planar imaging setups based on both μ PIV and background illumination with LEDs, only one double image high speed CMOS camera for each setup, a long-distance microscope and the associated visualization software, which provide an online measurement in high speed bubbly cavitation.

This thesis focuses on identification of hydrodynamic bubbly cavitation used for kidney stone treatment by acquiring the bubble size, shape and orientation on the basis of an accurate bubble image recognition algorithm using gradient-based image processing filters. This technique should be able to capture and analyze bubbles for all pressure values. However, capturing high speed bubbles in high frame rates causes extreme insufficient light from environment due to short exposure time so variable iris is employed in the camera system in order to ensure sufficient light condition. In addition, the same experimental set-up should provide the fluid phase velocity field with sub-pixel accuracy within a bubble swarm on the basis of PIV. This method needs an appropriate separation between images resulting from bubbles and tracer particles. Also, the bubble velocity should be determined with an object tracking algorithm. In order to achieve this, a solution consisting of three steps is produced: image acquisition, detection and analysis. In the first step a high speed CMOS camera system with a long distance microscope illuminated by LEDs is designed and a μ PIV setup in which another CMOS camera mounted to the body of a microscope is used. Thanks to the variable iris the micro-bubbles can be captured despite the insufficient environment light. Secondly, image processing algorithms are used for the purpose of

object recognition. Incremental self-tuning particle filtering (ISPF) is exploited in order to track cavitating bubbles in the third part.

1.2 Structure of the Thesis and Contributions

The thesis is organized as follows:

Chapter 2 reviews the most commonly used PIV and other image acquisition techniques for the measuring micro/nano particles velocity field, size and shape. Specific attention is dedicated to μ PIV and gradient based detection algorithms because they will be applied in subsequent chapters. Moreover, most common computer vision methods, tracking algorithms used in object tracking and medical application of cavitation types are described.

Chapter 3 proposes an imaging and detection framework for visualization and analysis of high speed cavitating bubbles. LED based illumination system and a long distance microscope are integrated to increase the resolution of the recorded image. Moreover, hydrodynamic cavitation system optimization of the effects of probe-to specimen distance on erosion rate of kidney stones are presented.

Chapter 4 describes the experimental and computational results obtained from the work presented in Chapter 3.

Chapter 5 presents conclusion of the thesis and discusses possible future works.

Contributions of the thesis can be listed as follows:

- A comprehensive high speed visualization method with LED based illumination that acquires high speed cavitating bubbles using dedicated image processing software is conducted. A variable iris is used for insufficient light conditions.
- A μ PIV setup is customized by Lab-on-a-Chip and used for high level visualization using a powerful laser system.

- Extensive computer vision analysis is performed by the utilization of several image processing algorithms in order to detect the micro bubbles and define their shape, size and orientation.
- Optimization and analysis of the high speed hydrodynamic cavitation system is accomplished.

Chapter II

2 Background

Recently, quantitative flow visualization has become an essential tool for investigating complex flow structures. Recent advances in laser, computer and digital image processing techniques have made it possible to extract velocity field information from visualized flow images of tracer particles. Particle image velocimetry (PIV)/particle tracking velocimetry (PTV) method has become one of the most useful flow diagnostic technologies in the modern history of fluid mechanics. The particle-based velocimetry techniques measure the whole velocity field information in a plane by dividing the displacements ΔX and ΔY of tracer particles with the time interval Δt during which the particles were displaced. Since the flow velocity is inferred from the particle displacement, it is important to select pertinent tracer particles that follow the flow motion accurately without changing the flow properties.

2.1 Visualization Techniques

2.1.1 Particle Image Velocimetry

PIV (Fig. 2.1) is a non-intrusive, whole-field optical technology used to obtain velocity data on "seeding" particles in a fluid in motion. It is based on the measurement of particle displacement over a known time interval. Thereby (particle) velocity is calculated according to the relationship:

$$Speed [m/s] = \frac{Distance[m]}{Time[s]} \quad (2.1)$$

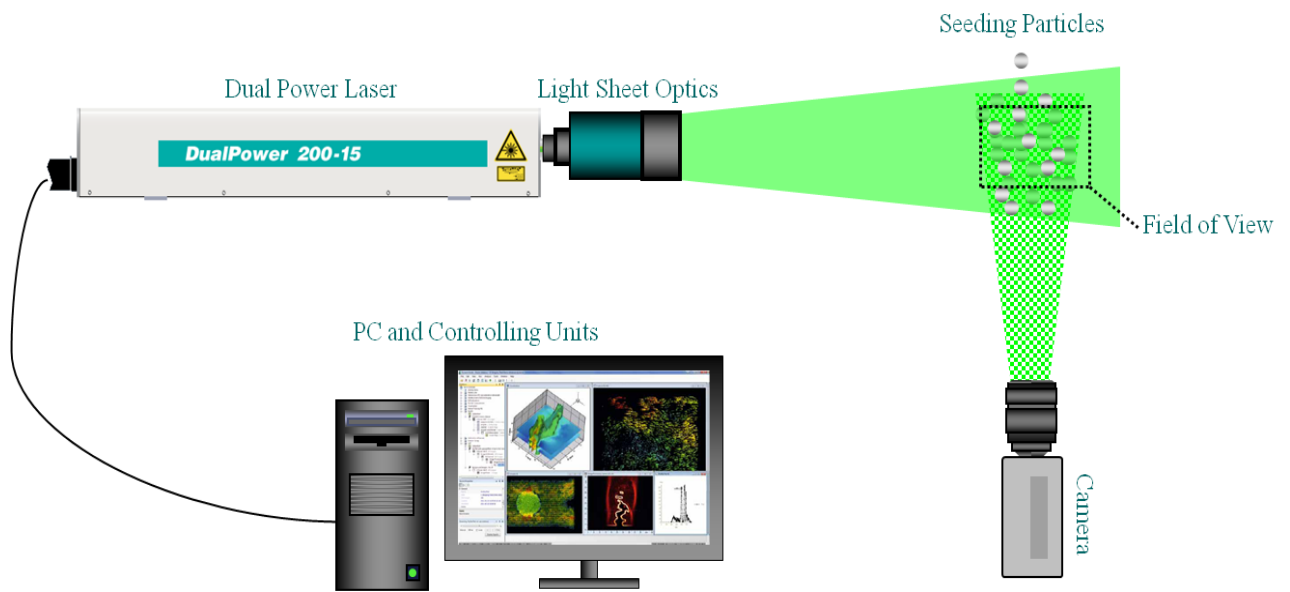


Figure 2.1: Particle Image Velocimetry (PIV) Configuration

Figure 2.2 briefly sketches a typical setup for PIV recording. Small tracer particles are added to the flow. A plane (light sheet) within the flow is illuminated twice by means of a laser (the time delay between pulses depending on the mean flow velocity and the magnification at imaging). It is assumed that the tracer particles move with local flow velocity between the two illuminations. The light scattered by the tracer particles is recorded “via a high quality lens” either on a single frame (e.g. on a high-resolution digital or film camera) or on two separate frames on special cross-correlation digital cameras. After development the photo-graphical PIV recording is digitized by means of a scanner. The output of the digital sensor is transferred to the memory of a computer directly.

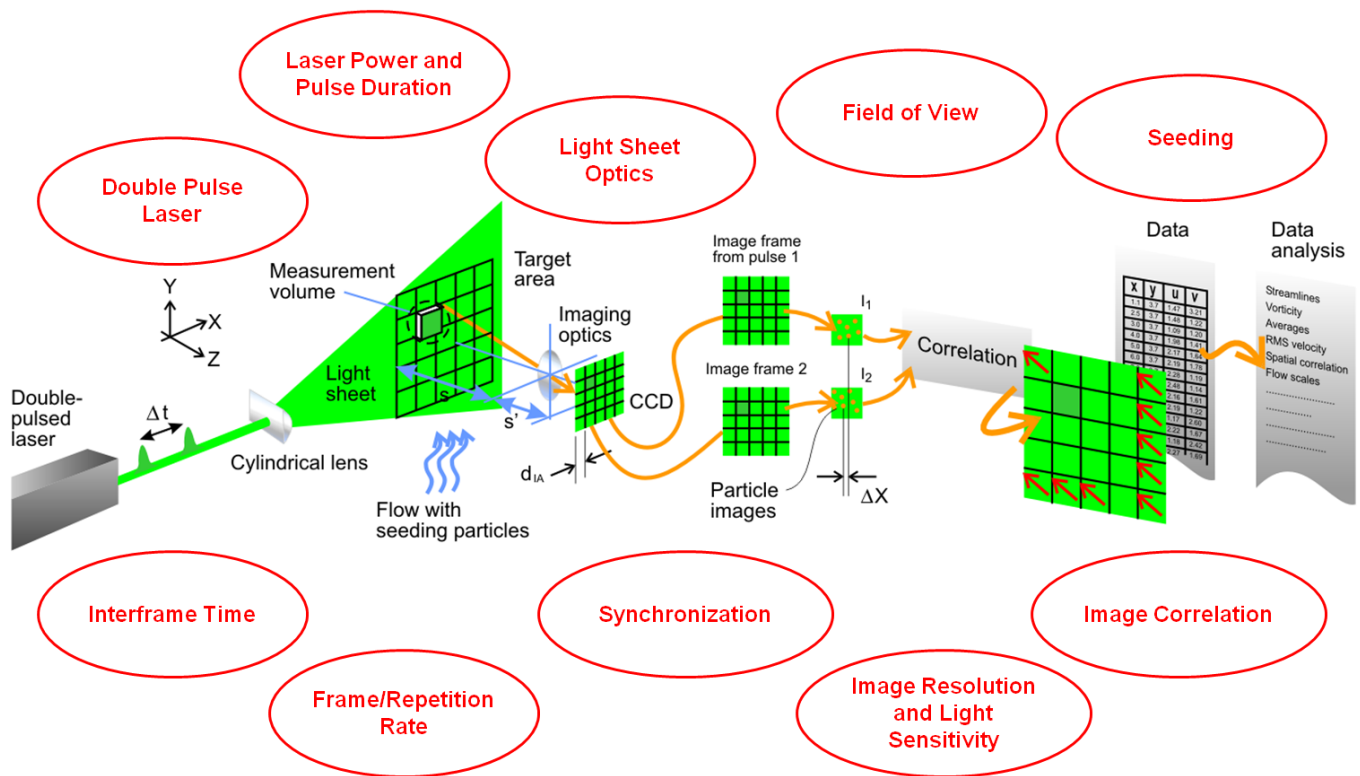


Figure 2.2: Particle Image Velocimetry (PIV) Principle

The main features of PIV indicated by Raffel et al. [44] as follows:

Non-intrusive velocity measurement. In contrast to techniques for the measurement of flow velocities employing probes such as pressure tubes or hot wires, the PIV technique being an optical technique works non-intrusively. This allows the application of PIV even in high-speed flows with shocks or in boundary layers close to the wall, where the flow may be disturbed by the presence of the probes.

Indirect velocity measurement. In the same way as with laser Doppler velocimetry the PIV technique measures the velocity of a fluid element indirectly by means of the measurement of the velocity of tracer particles within the flow, which in most applications have been added to the flow before the experiment starts. In two phase flows, particles are already present in the flow. In such a case it will be possible to measure the velocity of the particles

themselves as well as the velocity of the fluid (to be additionally seeded with small tracer particles).

Whole field technique. PIV is a technique which allows to record images of large parts of flow fields in a variety of applications in gaseous and liquid media and to extract the velocity information out of these images. This feature is unique to the PIV technique. Aside from Doppler Global Velocimetry (DGV, also known as “Planar Doppler Velocimetry”) [45], which is a new technique particularly appropriate for medium to high-speed air flows, and Molecular Tagging Velocimetry (MTV) all other techniques for velocity measurements only allow the measurement of the velocity of the flow at a single point, however in most cases with a high temporal resolution. The spatial resolution of PIV is large, whereas the temporal resolution (frame rate of recording PIV images) is limited due to current technological restrictions. These features must be kept in mind when comparing results obtained by PIV with those obtained with traditional techniques. Instantaneous image capture and high spatial resolution of PIV allow the detection of spatial structures even in unsteady flow fields.

Velocity lag. The need to employ tracer particles for the measurement of the flow velocity requires us to check carefully for each experiment whether the particles will faithfully follow the motion of the fluid elements, at least to that extent required by the objectives of the investigations. Small particles will follow the flow better.

Illumination. For applications in gas flows a high power light source for illumination of the tiny tracer particles is required in order to well expose the photographic film or the video sensor by scattered light. However, the need to utilize larger particles because of their better light scattering efficiency is in contradiction to the demand to have as small particles as possible in order to follow the flow faithfully. In most applications a compromise has to be found.

Duration of illumination pulse. The duration of the illumination light pulse must be short enough to “freeze” the motion of the particles during the pulse exposure in order to avoid blurring of the image (“no streaks”).

Time delay between illumination pulses. The time delay between the illumination pulses must be long enough to be able to determine the displacement between the images of the tracer particles with sufficient resolution and short enough to avoid particles with an out-of-plane velocity component leaving the light sheet between subsequent illuminations.

Distribution of tracer particles in the flow. At qualitative flow visualization certain areas of the flow are made visible by marking a stream tube in the flow with tracer particles (smoke, dye). According to the location of the seeding device the tracers will be entrained in specific areas of the flow (boundary layers, wakes behind models, etc.). The structure and the temporal evolution of these structures can be studied by means of qualitative flow visualization. For PIV the situation is different: a homogeneous distribution of medium density is desired for high quality PIV recordings in order to obtain optimal evaluation. No structures of the flow field can be detected on a PIV recording of high quality.

Density of tracer particle images. Qualitatively three different types of image density can be distinguished [43]. In the case of low image density, the images of individual particles can be detected and images corresponding to the same particle originating from different illuminations can be identified. Low image density requires tracking methods for evaluation. Therefore, this situation is referred to as “Particle Tracking Velocimetry”, abbreviated “PTV”. In the case of medium image density, the images of individual particles can be detected as well [72].

2.1.2 Particle Shadow Sizer (PSS)

High-magnification Shadow Imaging is very suitable for visualizing particles, droplets and other structures. The technique is based on high resolution imaging with pulsed backlight illumination. The measurement volume is defined by the focal plane and the depth of field of the imaging system. This technique is independent of the shape and material (either transparent or opaque) of the particles and allows the investigation of sizes down to the microscale using an appropriate optical system.

The light source can be a pulsed laser with special illumination optics or a flash lamp, depending on the velocity of the particles. Using a short laser pulse as illumination, it is possible to "freeze" motions of more than 100 m/s. A double pulse laser combined with a double frame camera allows the investigation of size dependent particle velocities [72].

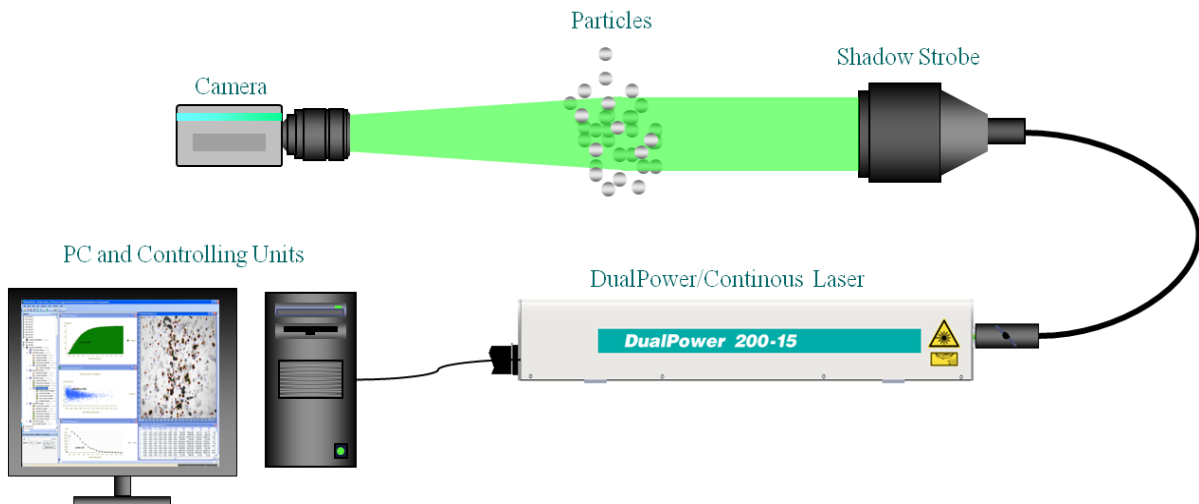


Figure 2.3: PSS Configuration

2.1.3 Phase Doppler Anemometry (PDA)

In its simplest and most presently used form, LDV crosses two beams of collimated, monochromatic, and coherent laser light in the flow of the fluid being measured. The two beams are usually obtained by splitting a single beam, thus ensuring coherence between

the two. Lasers with wavelengths in the visible spectrum (390–750 nm) are commonly used; these are typically He-Ne, Argon ion, or laser diode, allowing the beam path to be observed. A transmitting optics focuses the beams to intersect at their waists (the focal point of a laser beam), where they interfere and generate a set of straight fringes. As particles (either naturally occurring or induced) entrained in the fluid pass through the fringes, they reflect light that is then collected by a receiving optics and focused on a photo detector (typically an avalanche photodiode).

The reflected light fluctuates in intensity, the frequency of which is equivalent to the Doppler shift between the incident and scattered light, and is thus proportional to the component of particle velocity which lies in the plane of two laser beams. If the sensor is aligned to the flow such that the fringes are perpendicular to the flow direction, the electrical signal from the photo detector will then be proportional to the full particle velocity. By combining three devices (e.g.; He-Ne, Argon ion, and laser diode) with different wavelengths, all three flow velocity components can be simultaneously measured [72].

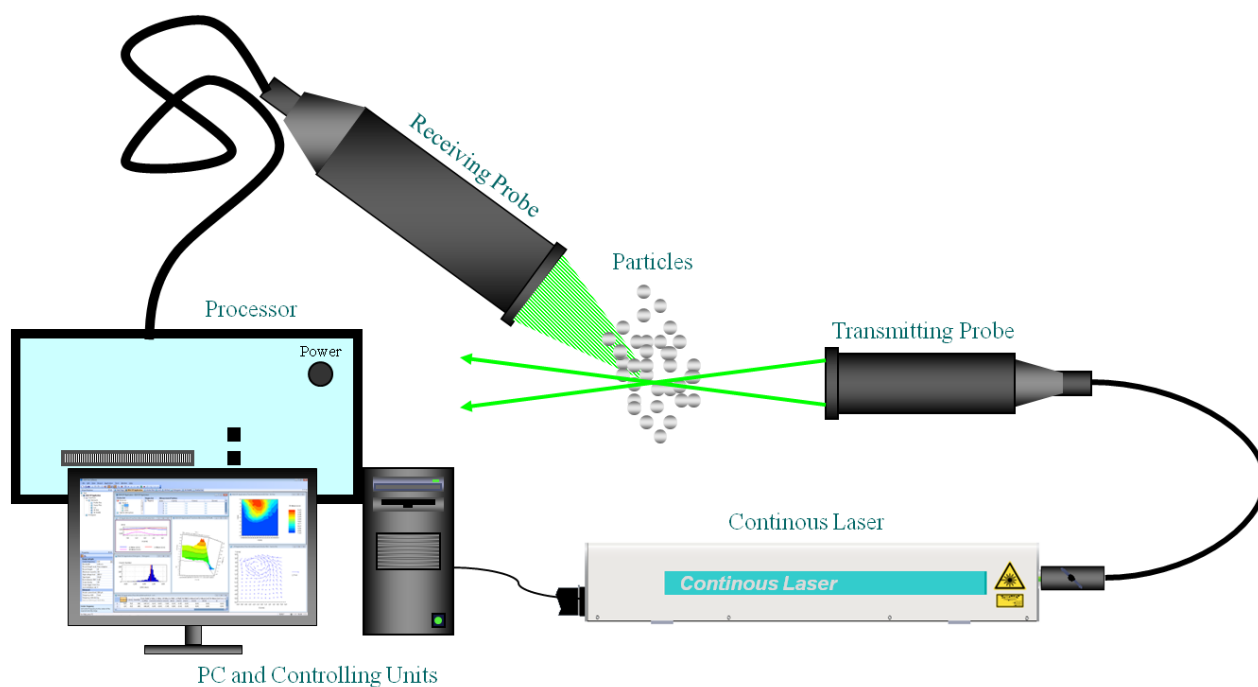


Figure 2.4: PDA Configuration

2.1.4 Interferometric Particle Imaging (IPI)

The technique implemented in the FlowMap Particle Sizer (FPS) software utilises the interferometric pattern created by a particle illuminated by a laser sheet. This technique has been given different names by different authors: Planar Mie Scattering Interferometry; Mie Scattering Imaging, Planar Interferometric Imaging, Interferometric light Imaging for Droplets Sizing or Interferometric Particle Imaging. In this manual we have selected the last, in abbreviated form known as IPI.

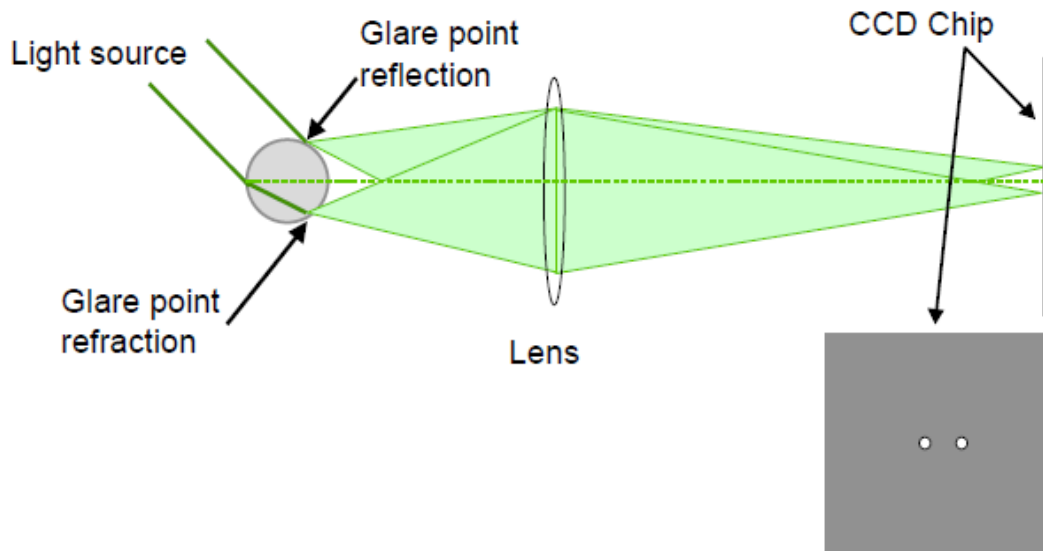


Figure 2.5: Generation of the two Glare points by a transparent particle

An in-focus image of a transparent particle illuminated by a coherent laser sheet will consist of two bright spots. These spots, or glare points, are coming from the reflected light on the surface of the particle and from the refracted light inside the particle (Fig. 2.5). For perpendicular polarisation, the camera should be located around $\phi=68$ deg, and for the parallel polarisation it should be located at $\phi=90$ deg (Fig. 2.6) [72].

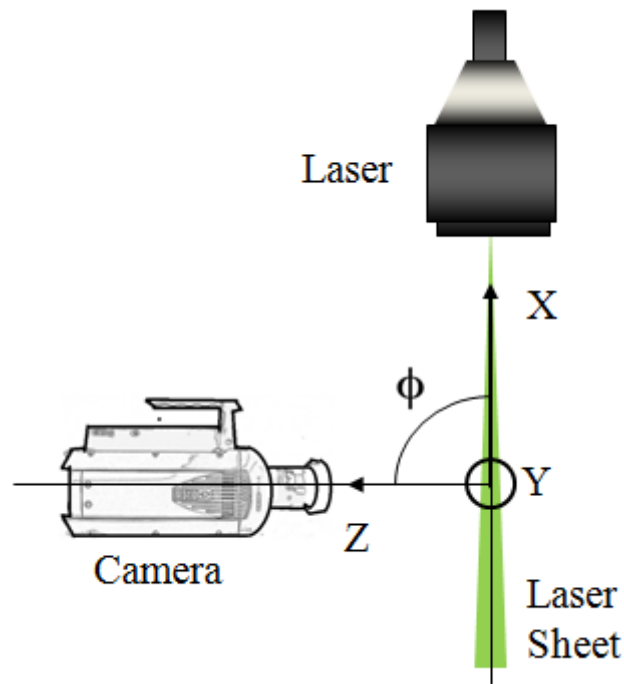


Figure 2.6: IPI Optical Configuration, Φ is the scattering angle or observation angle

2.2 Image Processing Techniques

Images are taken into account as one of the most essential methods of transferring data, in the area of computer vision, by comprehending images the data obtained from them can be utilized for various tasks for instance: navigation of robots, extracting harmful tissues from body scans, recognition of cancerous cells, and identification of an airfield from remote sensing information. In order to comprehend images, for example: acquiring detailed data such as colour, texture, number, and object recognition, image segmentation is the principal method. Therefore, image segmentation is the initial phase in image analysis. Occasionally image processing for noise removal is performed before the segmentation to avoid from the false contour detection for segmentation to divide the image without loss of data in biomedical applications is a challenging task.

2.2.1 Image Segmentation

Nowadays, based on various technologies, image segmentation methods are categorised as follows according to two properties of an image:

- **Detecting Discontinuities**

It proposes to divide an image regarding sudden changes in intensity [46], this comprises image segmentation algorithms such as edge detection.

- **Detecting Similarities**

It proposes to divide an image into sections that are alike regarding a group of predefined criteria [46]; this comprises image segmentation algorithms such as thresholding, region growing, region division and merging.

2.2.1.1 Segmentation Based on Edge Detection

This technique tries to perform image segmentation by detecting the edges or pixels between various sections that have fast alteration in intensity are determined [46, 50] and connected to generate closed object boundaries. The output is a binary image [47]. According to theory, two main edge based segmentation methods are present; gray histogram and gradient based method [49].

2.2.1.2 Thresholding Method

Image segmentation by thresholding is an easy but robust method for the segmentation of images that have bright objects on dark background [46]. Thresholding method is based on image-space areas i.e. on features of image [49]. Thresholding procedure changes a multi-level image into a binary image i.e., it determines an accurate threshold T , to partition image pixels into several sections and extract objects from background. Any pixel (x, y) is taken into account as a part of object if its intensity is greater than or equal to threshold value i.e., $f(x, y) \geq T$, else pixel pertains to background [48, 56]. For each selection of thresholding value, two types of thresholding approaches are present [57], global and local thresholding.

When T is constant, the method is called global thresholding or else it is called local thresholding. Global thresholding techniques can fail when the background illumination is irregular. In local thresholding, multiple thresholds are utilized to compensate for irregular illumination [53]. Naturally, threshold selection is conducted interactively however, it is possible to obtain robust threshold selection algorithms.

Constraint of thresholding technique is that, only two classes are produced, and it cannot be performed to multichannel images. Additionally, thresholding does not consider the spatial features of an image because of noise sensitivity [49], as both of these artefacts distort the image histogram, causing a more challenging separation.

2.2.1.3 Region Based Segmentation Method

In contrast to edge detection approach, segmentation algorithms based on region are rather easy and more robust to noise [49, 51]. Edge based techniques segment an image based on rapid alterations in intensity in the vicinity of edges whereas region based methods, segment an image into sections that are similar regarding a group of predefined criteria [55, 46].

2.2.1.4 Segmentation Methods Based on PDE (Partial Differential Equation)

Performing a PDE based method & explaining the PDE equation by a numerical scheme, image segmentation can be done. Image segmentation based on PDEs is mostly conducted by active contour model or snakes. This technique was first introduced by Kass et al. in 1987 [58] Kass improve this technique to obtain similar objects in existence of noise and other uncertainties. The main idea of snake is transformation of a segmentation problem into a PDE framework.

That is, the development of a given curve, surface or image is processed by PDEs and the solution of these PDEs is what we look forward to several techniques for image segmentation are - snake, level set and Mumford-shah model[73].

2.2.2 Morphology

The term morphology indicates the description of the properties of shape and formation of any objects. In the perspective of computer vision, this term stands for the description of the features of shapes of regions on the image. Procedures of mathematical morphology were initially described as procedures on sets, but it quickly became obvious that they are also effective in the operating tasks of the set of points in the two-dimensional space [59]. Sets in mathematical morphology correspond to objects in the image. It is simple to notice that the set of all background pixels of binary image is one of the alternatives for a full explanation. First of all mathematical morphology is utilized to extract some features of the image, effective for its presentation and identification, for instance; contours, skeletons and convex hulls. Moreover morphological techniques are performed in the beginning and final image processing, for instance, morphological filtering, thickening or thinning. The input data for the mathematical morphology are the two images: processed and particular, based on the type of procedures and solve problems. Such a particular image called primitive or structural element. Naturally, a structural element is much smaller than the processed image. Structural component can be regarded as an identification of the region with some form. It is obvious that the shape can be random, on condition that it can be represented as a binary image of a given size.

2.3 Object Tracking Techniques

Many methods have been suggested for visual tracking. An exhaustive study is revealed in [60]. They try to solve the tracking problem generally from two different aspects: novel appearance models, such as [60]–[64], or novel tracking strategies, such as [65]–[67]. Once a perfect appearance model (i.e., absolutely distinguishing, computationally effective, adaptive, etc.) is accessible, a simple strategy [e.g., standard particle filtering (PF) [65]] will result in very good tracking outputs. Although several tracking methods may seem very different, they can be roughly divided into two categories: the deterministic model [67–68] and the stochastic model [66, 69]. A deterministic model often approximates the position of the target straightforwardly from low-level characteristics by a gradient descent search to a cost function or by online learning. In contrast to the deterministic model, the stochastic model considers the measurement and model uncertainties during tracking procedure. This method generally formulates tracking as a problem of Bayesian inference in state space.

2.4 Cavitation Techniques

2.4.1 Hydrodynamic Cavitation

While hydrodynamic cavitation has been extensively studied in applications with hydromachinery, potential biomedical applications were recently considered as an emerging research area particularly in micro scale. Although there are many studies on ultrasound cavitation in treatments such as kidney stone treatment, side effects of ultrasound cavitation motivated researchers to seek for different, local and efficient methods such as hydrodynamic cavitation. Kosar et al. [25] investigated the effect of bubbly cavitating flows on chalk specimens and cell cultures and studied the impact of released bubbles on kidney chalk specimens and cancerous cells (Fig. 2.7). Their experimental setup did not include any moving part, and their experiments were carried out at various inlet pressures while

visualizing bubbly cavitating flow patterns. As the exposure times increased, more cancerous cells died, and a significant reduction in cell livability occurred after cavitation exposure. Perk et al. [27] conducted experiments on 18 kidney stone samples made of calcium oxalate and used phosphate buffered saline (PBS) solution as the working fluid. At a cavitation number of 0.017 and a probe to specimen distance of 1 mm, their experiments resulted in an erosion rate of 0.31 mg/min. Palanker et al. [28] used a two-dimensional Rayleigh-type hydrodynamic simulation in order to study the interaction between a jet containing bubbles and a soft tissue made of chorioallantoic membrane (CAM). They tried to avoid of generating cavitation bubbles, which might have considerable damage on the tissue using concave end probes. Their results were obtained under the condition of a maximum velocity of 80 m/s and tissue distance up to 1.4 mm. They showed that concave endoprobes can be used to prevent the tissue damage by slowing down the bubble back boundary diffusion. There are many studies focusing on hydrodynamic interactions among bubbles nearby the [29-32]. It was reported that cavitation phenomenon including formation, development and finally collapse, increased fragmentation due to tissue damage [33]. Itah et al. [26] used the setup of their previous work to investigate the effect of hydrodynamic cavitation on prostate cells and benign prostatic hyperplasia (BPH) tissue. The micro-orifice used in this experimental study was a polyether ether ketone (PEEK) with an inner diameter of 147 μm , while the pressure at the inlet was varied from 50 to 150 psi for cell culture experiments, and the physiological solution was Phosphate buffered saline (PBS). The size of the captured cavitation bubbles was between 60 to 300 μm . Their results on Prostate cancer cells PC-3 and DU-145 exposed to bubbly cavitation proved the destructive effect of hydrodynamic cavitation on prostate cells. However, there was no evidence of the damage in the DNA and activation of programmed cell death mechanisms. Their results indicated that cavitation damaged cells instantly and pulverized cells upon

exposure. They claimed that hydrodynamic cavitation could be a viable alternative to ultrasound cavitation in treatments involving BPH tissues.

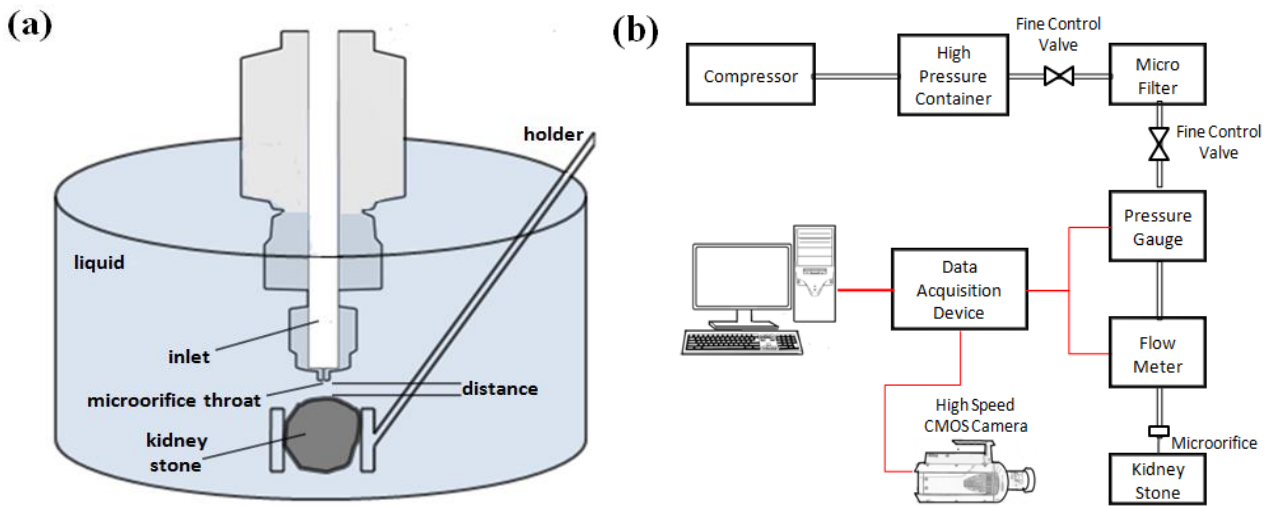


Figure 2.7: (a) Microchannel configuration with the orifice throat and exit area and experimental placement of the kidney stone (b) Experimental setup

2.4.2 Ultrasound Cavitation

Ultrasound cavitation has many applications in biomedical engineering. Drug delivery systems are one of such applications, which exploit ultrasound methods to treat the natural barrier function of the skin [34]. Sonophoresis as a feature of the ultrasound method is used to enhance the performance of drug delivery systems. It is well-known that the shock wave lithotripsy is an effective biomedical treatment especially in stone fragmentation and includes two fundamental mechanisms, namely shock wave and cavitation phenomenon. Mechanical stresses generated by shock wave lithotripsy lead to stone fragmentation [38]. There are many studies in the literature on shock wave lithotripsy, and many researchers proposed new methods to enhance the effectiveness of shock wave lithotripsy by intensifying shock waves. Preliminary studies focused on the capability of SWL and ultrasound cavitation for stone combination. Sass et al. [39] used kidney stones and

gallstones exposed to shock waves and reported a two-step process in resulting erosion. They showed that first slits formed as a result of the interaction between shock wave and targets and then the liquid fills small cracks at the first step, and secondly, the collapse with cavitation causes significant erosion on the surface of stones, and finally, fragmentation takes place. Holmer et al. [40] also showed that acoustic cavitation and streaming had significant effects on the disintegration of stones.

It was proven in many studies that extracorporeal shock wave therapy could affect coronary angiogenesis and enhanced myocardial ischemia in patients with intense coronary artery disease [41]. This method had a significant impact on medicating ischemic heart diseases. The relationship between shock wave lithotripsy and cavitation was investigated by Smith et al [42]. They performed several in vitro experiments at the acoustic field of electromagnetic SWL with different fluids in order to determine the role of cavitation. Their results revealed that the type of the stone (hard or soft) changed the thresholds in average peak pressures.

Chapter III

3 Quantification of Cavity Bubbles Using a High Speed Camera System with LED Based Illumination

In this chapter, we propose a comprehensive visualization and image analysis of high speed hydrodynamic cavitation work using a high speed imaging system and robust vision modules. In the concept of imaging high speed micro fluids, some undesired phenomena such as insufficient light, out of focus bubble or some ergonomically inadequate visualization system-experimental setup integration might occur. With the proposed work, these problems are eliminated by the usage of a long-distance microscope with a variable iris. Long-distance microscope ensures the integration of the setup with high speed CMOS camera system without existence of a Lab-on-a-chip.

3.1 Visualization System and Image Acquisition

In the experiments, the images of the two phase flow are captured by a double shutter CMOS camera (Phantom v310, a trademark of Vision RESEARCH), which is a high speed camera with 10,000 fps. The speed of the camera is 3 Gpx/second and maximum speed at full resolution of 1280 x 800 (20 μm pixel size) is 3,250 fps. The camera has a minimum frame rate of 24 fps. Blur can be eliminated and the minutest details can be seen by using short exposure times. On the v310, exposure time can be set to the minimum value of 1 microsecond. The camera supports 8- and 12-bit pixel depth. While smaller bit-depth implies more recording time and smaller files, greater bit-depth provides more gray levels and finer details. With the greater latitude of 12 bits, one can pull more details out of the

image.

Due to resolution and lighting issues, the camera is used at 3,250 fps, which provides reasonably good images. K2 DistaMax special lens, which offers ultimate in long-distance microscopy is utilized and positioned at a distance of 158 mm from the imaging plane. This optical procedure provides that only the central section of the lens is used where eccentricity is neglected. TX Tube of the lens provides amplification of $M = 2$ in all cases, with all objectives, and with all working distance choices. It should be noted that although the Phantom v310 camera has sensitivity needed for even the most challenging lighting conditions, throughout our experiments, because of the insufficient lighting in the environment we utilized a variable iris in our camera system. Besides the focusing ring, the K2 DistaMax has a built-in iris diaphragm for depth of field and light attenuation control.

The imaging system is equipped with 2 pulsed 198 high performance LED array have a total area of 180 mm × 120 mm for a background illumination. The average duration of the light pulses is approximately 60 μ s and the average time delay between the two consecutive images is attuned to the flow velocity 2 ms.

In order to perform offline evaluation (control and image processing) of the raw images, the captures are transferred digitally from the CMOS camera to the work station. The online evaluation of the images, which is important for a fully automated analysis at high resolution, is performed by the software written by Dantec Dynamics A/S. As a first step in image processing, the captures are changed into 8 bit format grey value image. Moreover, auto- optimization of the contrast and normalization of the greyscale values are conducted.

3.2 Image Processing of Microscale Bubbly Cavitation

3.2.1 Background Noise Removal

In order to reduce the effect of systematic noise and augment image contrast, background noise removal is essential. Median filtering is a nonlinear signal processing used to remove noise from images and widely performed as it is very effective at eliminating noise while preserving edges. It is especially useful at eliminating 'salt and pepper' type noise. The median filter works by a mask which slides through the image pixel by pixel, replacing the noisy value of the digital image with the median value of neighbouring pixels. The median is calculated by first sorting all the pixel values from the window into numerical order, and then replacing the pixel being considered with the middle (median) pixel value. The noisy value of the digital image is replaced by the median value of the mask, which is calculated by first sorting all the pixel values from the window into numerical order. The output of median filtering is $h(x, y) = \text{median}\{f(x - i, y - j), i, j \in W\}$ where $f(x, y)$, $h(x, y)$ are the original image and the filtered image, W is the 2D mask which has the size of $(2m+1)*(2m+1)$ pixels, where m is an integer and generally set to 2.

3.2.2 Image Enhancement

Cavity flow image with low brightness must be augmented to develop represent of the cavity bubble details. The histogram equalization is used to advance image illumination. Let f be a given image represented as a m_r by m_c matrix of integer pixel intensities ranging from 0 to $L-1$. L is the number of possible intensity values, often 256. Let p denote the normalized histogram of f with a bin for each of possible intensity. So

$$p_n = \frac{\text{number of pixels with intensity } n}{\text{total number of pixels}} \quad n = 0, 1, \dots, L - 1. \quad (3.1)$$

The histogram equalized image g will be defined by

$$g_{i,j} = \text{floor}((L - 1) \sum_{n=0}^{f_{i,j}} p_n) \quad (3.2)$$

Where $\text{floor}()$ rounds down to the nearest integer.

Then the contrast of image is improved by nonlinear γ -regulation mapping, in which the gray level of image is plotted to the range from 0 to 1, and the low gray level is condensed by the $\gamma=0.3$. The enhanced image is treated by the smoothing technology subsequently.

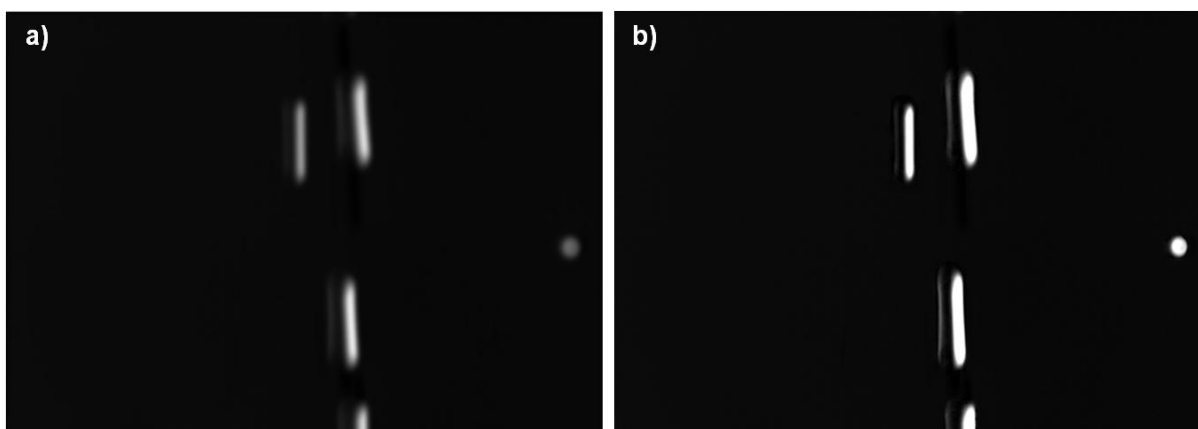


Figure 3.1: (a) Original image, (b) Image after histogram equalization

3.2.3 Morphological Image Processing

Although the cavity flow image is improved enough to reveal the shapes of bubbles, there are also noisy areas and non-cohesive boundary caused by the enhancement process. This leads to the cavity bubble recognition and image segmentation very difficult. To acquire continues boundary and enhance the quality of segmentation, morphology filtering is performed to eliminate the remaining noise and unfilled boundaries of the edge detecting

[46]. In theory, circular operator is much better for obtaining a smooth target boundary. But when the filtering operator is more than 4x4, the objects end up with large deformation in this research. Consequently, a four zero corner 4x4 operator is utilized to perform morphologically filtering with twice *erosion* and *dilation*.

$$Dilation \rightarrow D(A, B) = A \oplus B = \cup_{\beta \in B} (A + \beta) \quad (3.3)$$

$$Erosion \rightarrow E(A, B) = A \ominus (-B) = \bigcap_{\beta \in B} (A - \beta) \quad (3.4)$$

Where $-B = \{-\beta | \beta \in B\}$. In order to compare the boundary and original images, the two images are combined together.

3.2.4 Extracting Bubble Properties

3.2.4.1 Bubble Detection

In order to do a robust bubble detection, the gradient $S(x, y)$ of the grey value distribution was computed applying the convolution kernels $S_x(x, y)$ and $S_y(x, y)$:

$$S(x, y) = \sqrt{S_x^2(x, y) + S_y^2(x, y)} \quad (3.5)$$

$$S_x(x, y) : \begin{bmatrix} -1 & 0 & 1 \\ -2 & 0 & 2 \\ -1 & 0 & 1 \end{bmatrix}, \quad S_y(x, y) : \begin{bmatrix} -1 & -2 & -1 \\ 0 & 0 & 0 \\ 1 & 2 & 1 \end{bmatrix} \quad (3.6)$$

Therefore, in the bubble detection algorithm the gradient of the grey values of the edges of the cavity bubbles was employed as a criterion for validation. Edges are only accepted if the gradient value was more than a predetermined threshold level, which was optimized for

each calculation performed to generate the maximum bubble detection. After that, the recognized edge points were converted to a polar coordinate system with their centre points as the origin. Then the cavity bubble contour was discretized with about 33 to 66 section with an identical angle in order to adjust the computational effort. The existing number of contour points is usually much higher and determined by the resolution of the cavity bubble, thus the number of pixels positioned on the contour region. Hence, all contour points positioned in one contour component were put together to generate only one contour reference point for each component. This was reached by weighing all contour points $(x_{k,j}, y_{k,j})$ with the local gradient $S(x_{k,j}, y_{k,j})$. Thus, the contour reference point (x_i, y_i) for each contour component was achieved by

$$x_i = \frac{\sum_j x_{k,j} S(x_{k,j}, y_{k,j})}{\sum_j S(x_{k,j}, y_{k,j})}, \quad y_i = \frac{\sum_j y_{k,j} S(x_{k,j}, y_{k,j})}{\sum_j S(x_{k,j}, y_{k,j})} \quad (3.7)$$

The cross-sectional region of the cavity bubble is verified by a summation of the region of the triangular elements A_i which are illustrated by the working point (x_w, y_w) and two neighbouring contour points (x_i, y_i) and (x_{i+1}, y_{i+1}) :

$$A_B = \sum_{i=1}^{N-1} A_i = \sum \frac{1}{2} \begin{vmatrix} x_i & y_i & 1 \\ x_{i+1} & y_{i+1} & 1 \\ x_w & y_w & 1 \end{vmatrix} \quad (3.8)$$

The centroid of the cavity bubble cross-section (x_c, y_c) was achieved with the centers of gravity of the triangular components in the following way:

$$x_c = \frac{\sum A_i x_{s,i}}{\sum A_i}, \quad y_c = \frac{\sum A_i y_{s,i}}{\sum A_i} \quad (3.9)$$

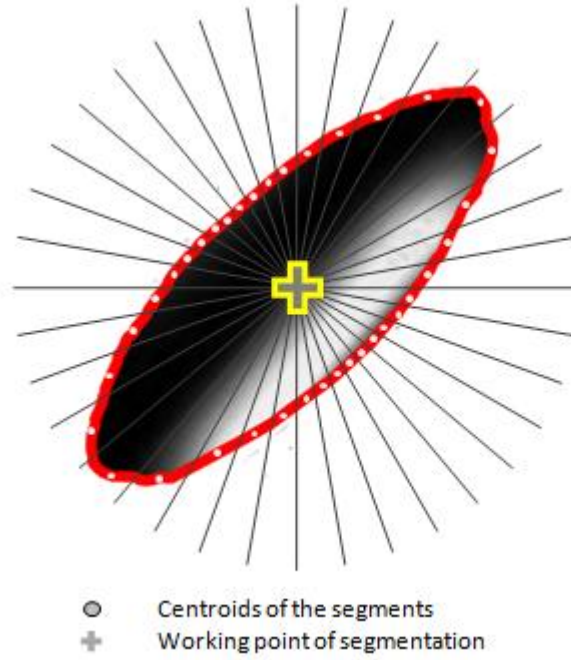


Figure 3.2: Segmentation of planar bubble image around a working point

3.2.4.2 Bubble Size Estimation

In this thesis, only a planar projection of the cavity bubbles is utilized to perform bubble characterization on the basis of detection and reconstruction algorithm explained previous section. Obviously, the precision of the diameter determination will be better for small firm and spherical cavity bubbles than for large ellipsoidal or vibrating cavity bubbles with powerful shape oscillations. The easiest technique to approximately calculate the cavity bubble volume V_B is to determine a bubble diameter D_A which is the region equivalent to the projection area A_{Pro} of a identified bubble:

$$A_{Pro} = \frac{\pi}{4} AB = \frac{\pi}{4} D_A^2 \quad (3.10)$$

where A and B are the major and minor axes of the spheroid with the eccentricity $\chi = A/B$ (figure 3.3). Thus, the cavity bubble volume is identical to the volume of a sphere with this region-equivalent diameter. Nevertheless, bubbles with region-equivalent diameters larger than $200\ \mu\text{m}$ have an eccentricity larger than 100 and differ significantly from a sphere [69]. These bubbles can be defined as spheroids and their volume is

$$A_{Spheroid} = \frac{\pi}{6}ABC \quad (3.11)$$

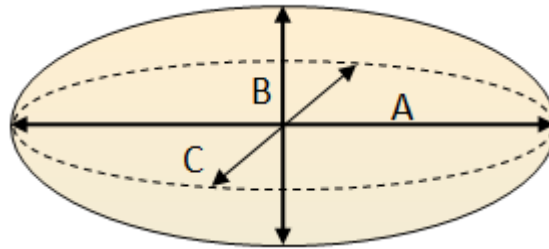


Figure 3.3: Spheroid with main axes (major axes A and C , minor axis B)

Both horizontal major axes A and C are approximately equivalent and larger than the vertical minor axis B for a spheroid. By a substitution of the major axis C , which was not computed, with the longest chord length of the bubble outline A , an prediction of the bubble volume V_B is proposed by the following equation:

$$V_B = \frac{\pi}{6}A^2B = \frac{\pi}{6}D_A^2 \cdot A \quad (3.12)$$

thus the region- and volume-equivalent cavity bubble diameters of a spheroid are

$$D_A = \sqrt{AB}, \quad D_V = (A^2B)^{\frac{1}{3}} \quad (3.13)$$

the calculated minor axis of the cavity bubble for a given orientation β is

$$B' = \sqrt{C^2 \sin^2 \beta + C^2 \cos^2 \beta} \quad (3.14)$$

where C is the major axis corresponding A and B is the correct minor axis of the spheroidal cavity bubble. Hence, the predicted region-equivalent cavity bubble diameter is given by

$$D'_A = \sqrt{AB'} = \sqrt{A\sqrt{A^2 \sin^2 \beta + B^2 \cos^2 \beta}} \quad (3.15)$$

3.3 Bubble Tracking

Tracking can be expressed as a Bayesian assumption task in a Markov model with hidden state variables, in the particle filtering (PF) environment;

$$p(\mathbf{X}_t | \mathbf{O}_t) \propto p(\mathbf{o}_t | \mathbf{X}_t) \int p(\mathbf{X}_t | \mathbf{X}_{t-1}) p(\mathbf{X}_{t-1} | \mathbf{O}_{t-1}) d\mathbf{X}_{t-1} \quad (3.16)$$

where \mathbf{X}_t identifies the state variable of the target object at time t and $\mathbf{O}_t = \{\mathbf{o}_1, \mathbf{o}_2, \dots, \mathbf{o}_t\}$ is a set of observations. The observation model $p(\mathbf{o}_t | \mathbf{X}_t)$ and the dynamic model $p(\mathbf{X}_t | \mathbf{X}_{t-1})$ between two states describe the procedure. State \mathbf{X} is a 2-D affine transformation matrix given as

$$\mathbf{X} = \begin{pmatrix} \mathbf{C} & \mathbf{e} \\ 0 & 1 \end{pmatrix} \quad (3.17)$$

where \mathbf{C} is a nonsingular 2×2 matrix and $\mathbf{e} \in \mathbb{R}^2$. All affine transformations generate the affine group (i.e., the matrix Lie group).



Figure 3.4: Example of subspace learned by the IPCA method

At frame #0, the initial state \mathbf{X}_0 is utilized to perform initial calculations of two distributions: target-patch similarity distribution (TSD) and background-patch similarity distribution (BSD) from appearance model. The similarity between a patch and learned appearance subspace is measured (Fig. 3.4). TSD is the similarity distribution of target patches (expressed by the states that contains the tracked target optimally), and BSD is the similarity distribution of background patches. TSD and BSD are estimated by Gaussian and are described by $\mathcal{N}_T(\mu_T, \sigma_T)$ and $\mathcal{N}_B(\mu_B, \sigma_B)$, respectively. Also, a pose estimator (PE) is used with a pose training group formed by making small variations around the initial state. At frame # t , the PF procedure incrementally draws/produces random samples on the affine group. After that it uses the PE to adjust them to their neighbouring optimal states. Sampling will be terminated if the maximum similarity score of all adjusted particles is larger than $\mu_T - \sigma_T$ or if the maximum number of particles is acquired. The condition of the target $\hat{\mathbf{X}}_t$ is approximated by the sample with the maximum similarity score \hat{S}_t . If the final maximum similarity score is good enough e.g., $\hat{S}_t > \mu_B + \sigma_B$, all online-learned

models will be updated according to the estimated state $\hat{\mathbf{X}}_t$. Then, a few of particles are sampled again from the adjusted particles and utilized as the initial particles for the next frame [70].

3.4 Hydrodynamic Cavitation Experimental Setup Optimization

Experimental erosion rate data in this study are used to develop a correlation providing the best prediction of the experimental data based on Curve Fitting using Least Squares Method. This correlation is based on the approach of Crowe [71], where the erosion rate is written in terms of important parameter, which are R_p (in mm), the particle radius (average bubble radius, taken as 90 μm in this study), σ_b (in Pa), the flexural strength, E_t (in Pa), the Young's modulus of elasticity, t (in min), time, dis (in mm), probe-specimen distance, and is expressed as:

$$W (mg/min) = E_t^{0.8} \sigma_b^2 R_p^{-1.19} 7074x10^4 ((-4.23)x10^{-11} dis^2 + (2.4)x10^{-10} dis - (1.01)x10^{-9}) ((4.22)x10^{-12} - (8.61)x10^{-14} t). \quad (3.18)$$

The above correlation can predict the experimental data with an MAE (Mean Absolute Error) of 6.09%. All of the experimental data are within 25% of the correlation as shown in Fig. 3.5. Spherical particles are considered as bubbles, while it was also assumed that micro bubbles emerging from the microprobe have the same velocity as the flow velocity inside the probe.

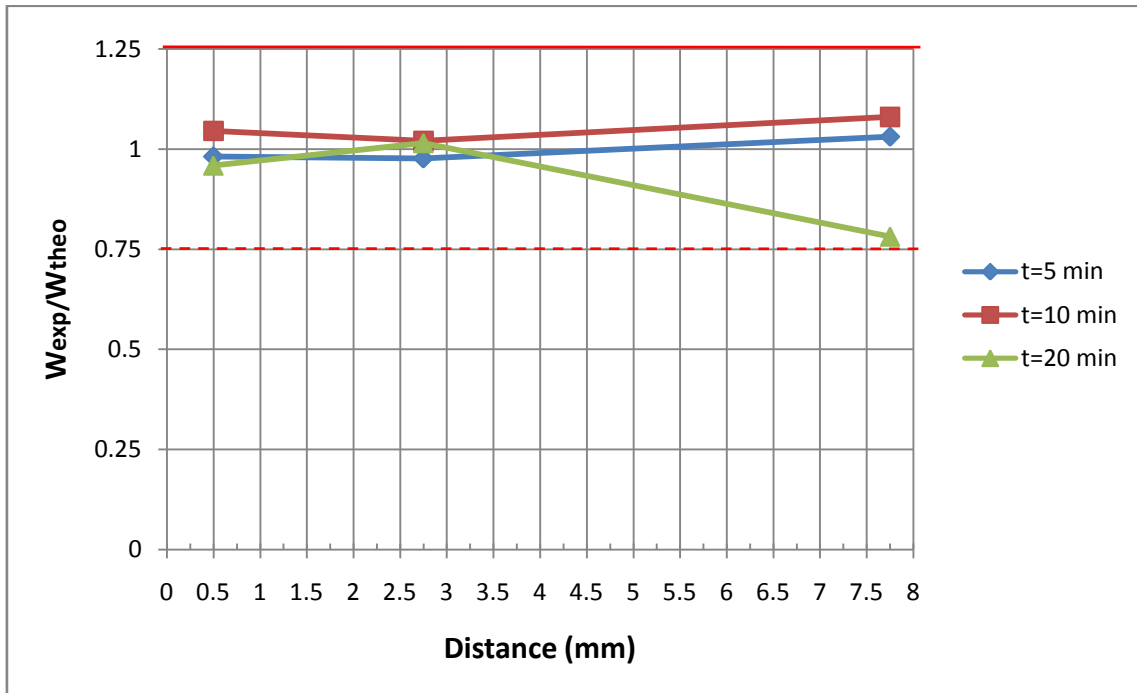


Figure 3.5 : Comparison of experimental erosion rate with predictions of the proposed correlation

Chapter IV

4 Experimental and Image Analysis Results

In this chapter, experimental results and image analysis, that are performed for Chapter 3 are provided, respectively.

4.1 Experimental Results

4.1.1 Experimental Setup

In the experiments, high resolution planar imaging system including a μ PIV and a CMOS camera (Phantom v310, a trademark of Vision RESEARCH), which is a high speed camera with 10,000 fps and illuminated by 2 pulsed 198 high performance LED array have a total area of 180 mm \times 120 mm, is used (Fig. 4.1). The speed of the camera is 3 Gpx/second and max. speed at full resolution of 1280 x 800 (20 μ m pixel size) is 3,250 fps. The camera has a minimum frame rate of 24 fps. Blur can be eliminated and the minutest details can be seen by using short exposure times. On the v310, exposure time can be set to the minimum value of 1 microsecond. The camera supports 8- and 12-bit pixel depth. While smaller bit-depth implies more recording time and smaller files, greater bit-depth provides more gray levels and finer details. With the greater latitude of 12 bits, one can pull more details out of the image.

Due to resolution and lighting issues, we used the camera at 3,250 fps, which provides reasonably good images. We also utilized K2 DistaMax special lens, which offers ultimate in long-distance microscopy. TX Tube of the lens provides 2x amplification in all cases, with all objectives, and with all working distance choices. It should be noted that although the Phantom v310 camera has sensitivity needed for even the most challenging lighting

conditions, throughout our experiments, because of the insufficient lighting in the environment we utilized a variable iris in our camera system. Besides the focusing ring, the K2 DistaMax has a built-in iris diaphragm for depth of field and light attenuation control.

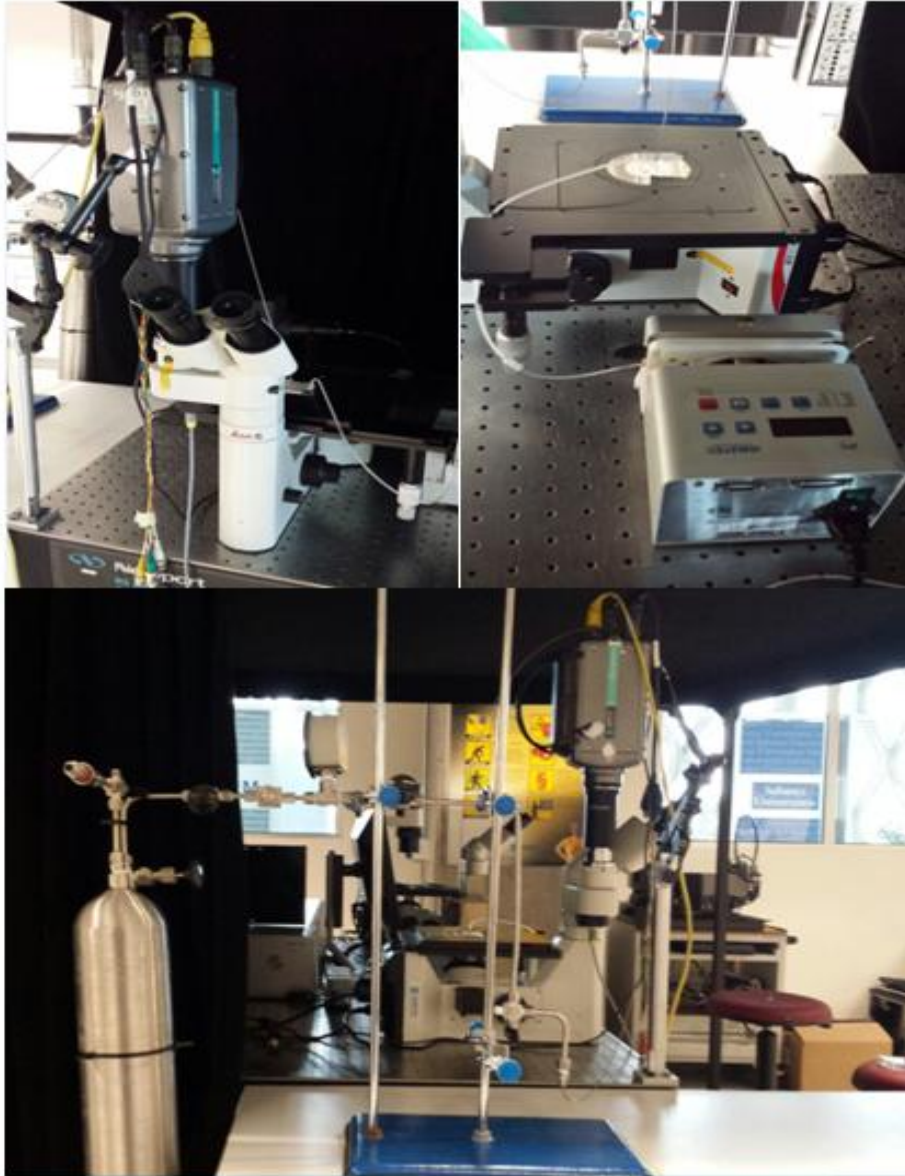


Figure 4.1 : Experimental Setup

4.1.2 Results for Image Acquisition

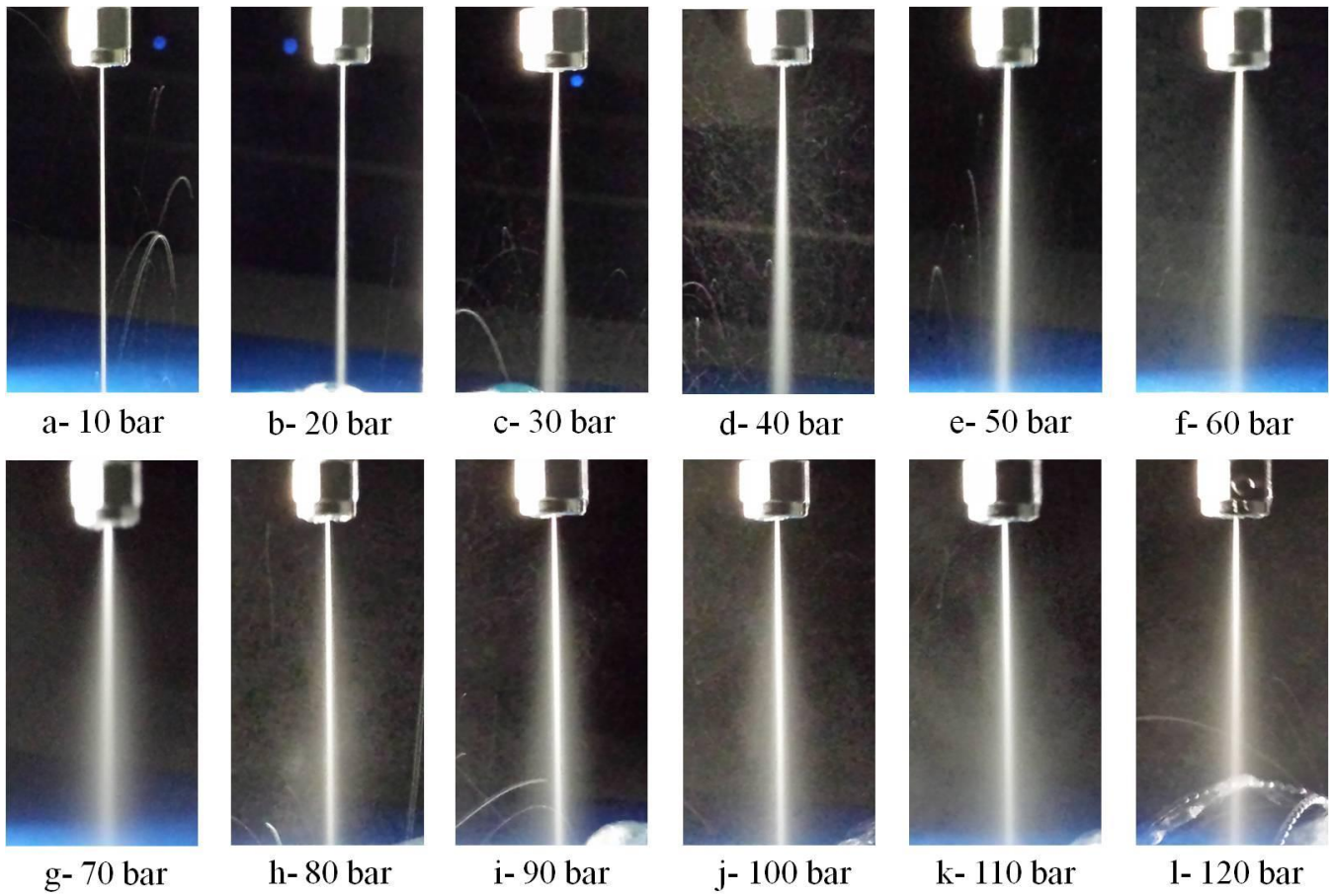


Figure 4.2 : Bubble cloud emerging from the probe exit at different cavitation intensities

In figure 4.2, it is obvious that different inlet pressures result in different penetration lengths (and accordingly different effective volumes), e.g. different maximum vertical distances measured from the probe, where cavitation effects can be observed.

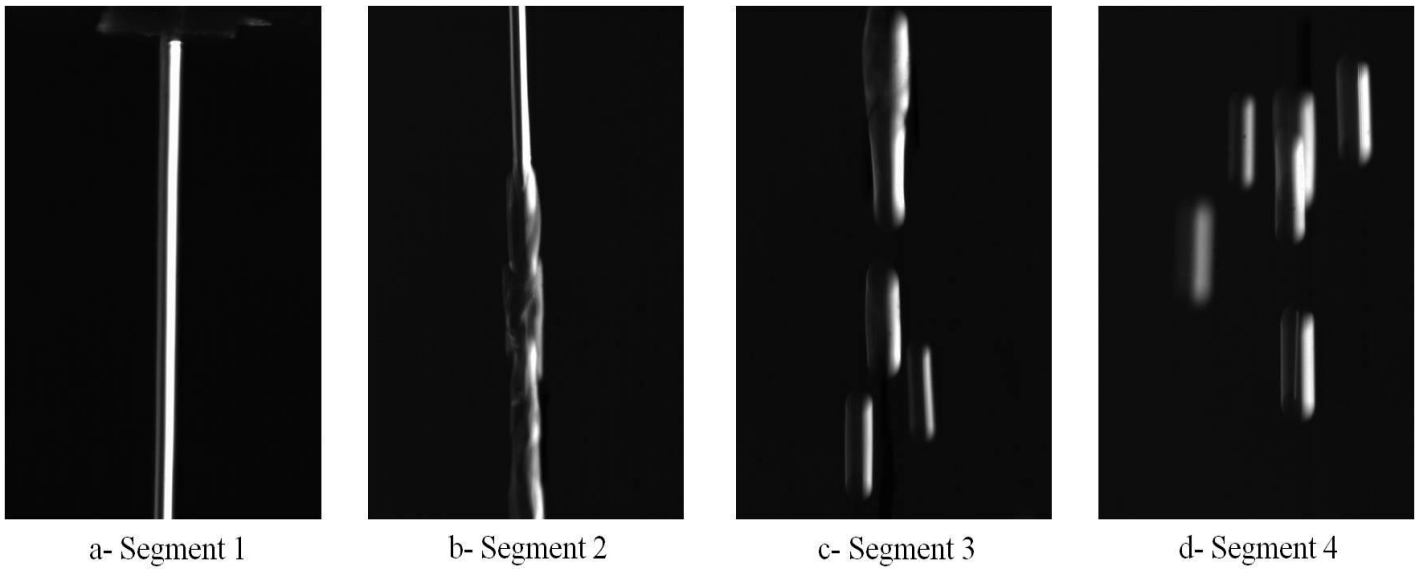


Figure 4.3 : Bubble cloud emerging that is captured through increasing distance from the probe exit, respectively

4.1.3 Results for Image Processing and Characterization of Cavity Bubbles

Due the low-level illumination, flow image processing is performed as follows; background noise removing, image enhancing, morphology filtering, and bubble identifying.

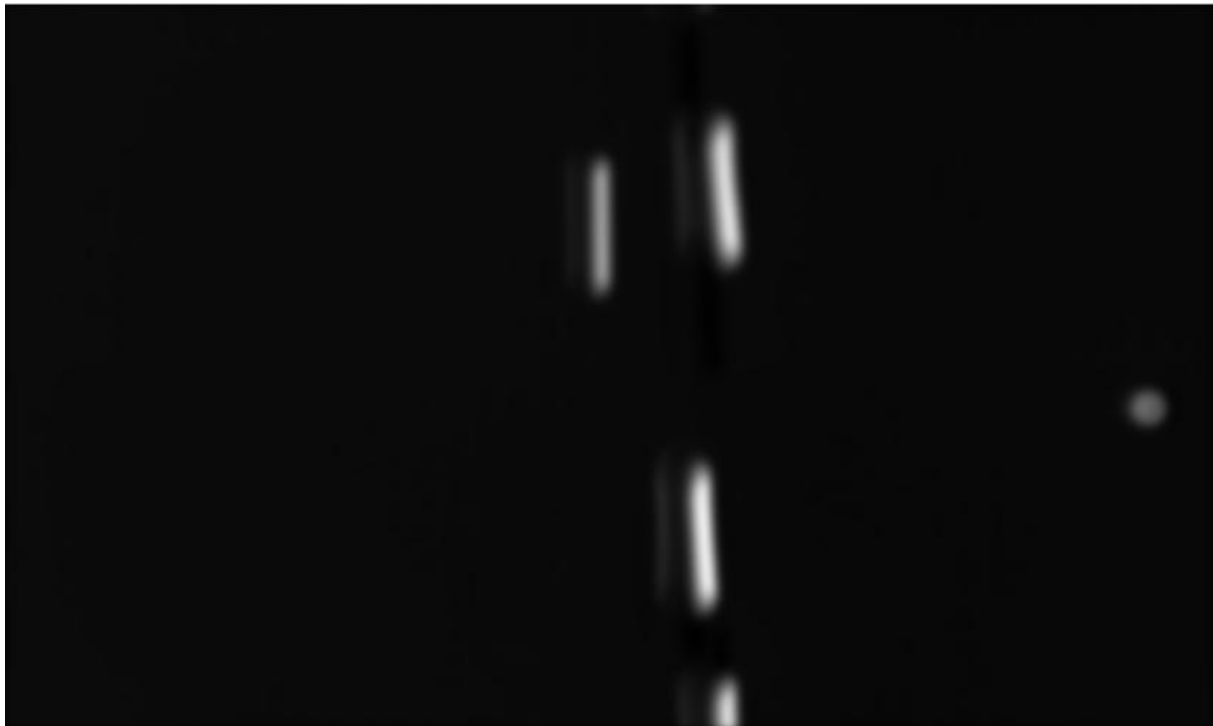


Figure 4.4 : Original flow image

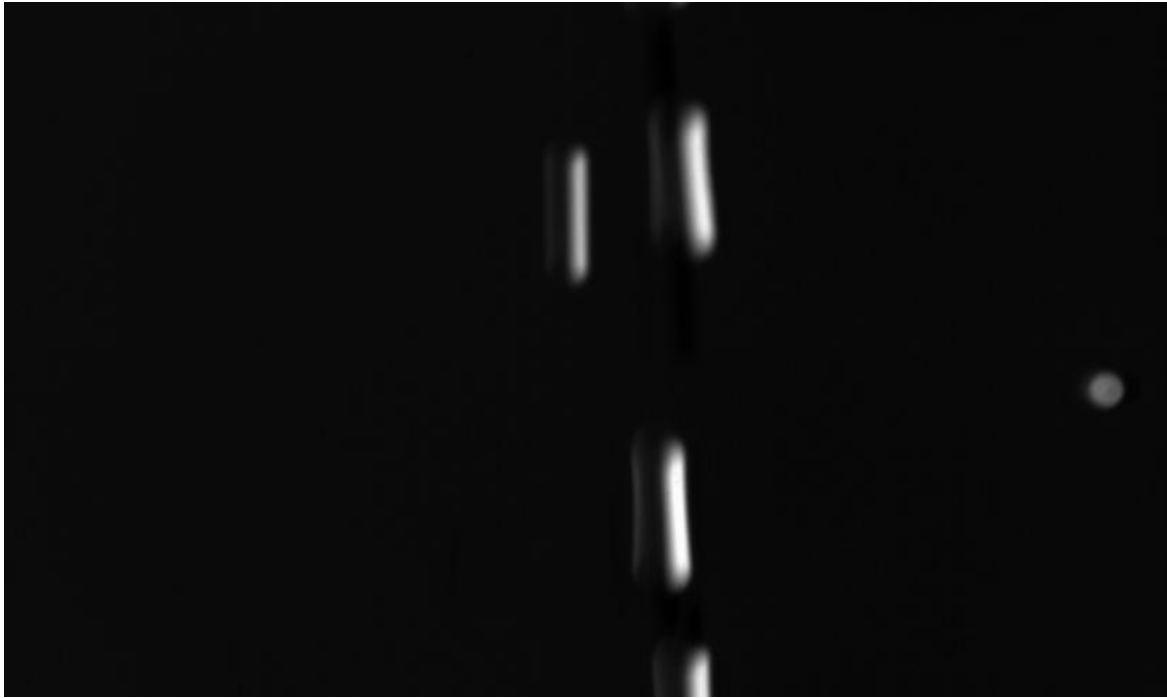


Figure 4.5 : Deblurred flow image

Eliminating background noise from original image plays an essential role in diminishing the effect of systematic noise significantly and enhancing image contrast. Due to the high frequency characteristic of background noise, high-pass filtering is utilized to deduct it from original image. First of all, the original image is subjected to FFT. Then, convolution operation with high-pass filtering is performed to filter high frequency noise element from the image. Finally, the filtered image is reconstructed by an inverse-FFT operation. The acquired image is low-intervention high speed bubbly flow image with low illumination. Fig. 4.4 a shows the original flow image, while Fig. 4.6 shows the noise filtered image. The previous image is so much noisy that it is hard to identify bubble from it, while the obtained image has a low illumination due to further lower brightness and contrast ratio.



Figure 4.6 : Flow image filtered for background noise removal

In order to obtain sharp images for cavity bubble detection, blur, which might occur in such microscopic images, must be removed. Blur could be the result of inappropriate imaging conditions such as out of focus camera, or relative motion of the camera and the imaged object. In order to remove or minimize the effect of the blur existing in the images, one can utilize a deblurring algorithm on the blurred images. Deblurring algorithms can be developed using either linear or non-linear filtering approaches. In this work, a linear deconvolution type deblurring algorithm is implemented. Blurred images are deconvolved with a filter (mask), which has the size of $(2m+1)*(2m+1)$ pixels, where m is an integer. In our implementations, we set $m=2$. The resulting enhanced images (Fig. 4.5) have sharper boundaries.

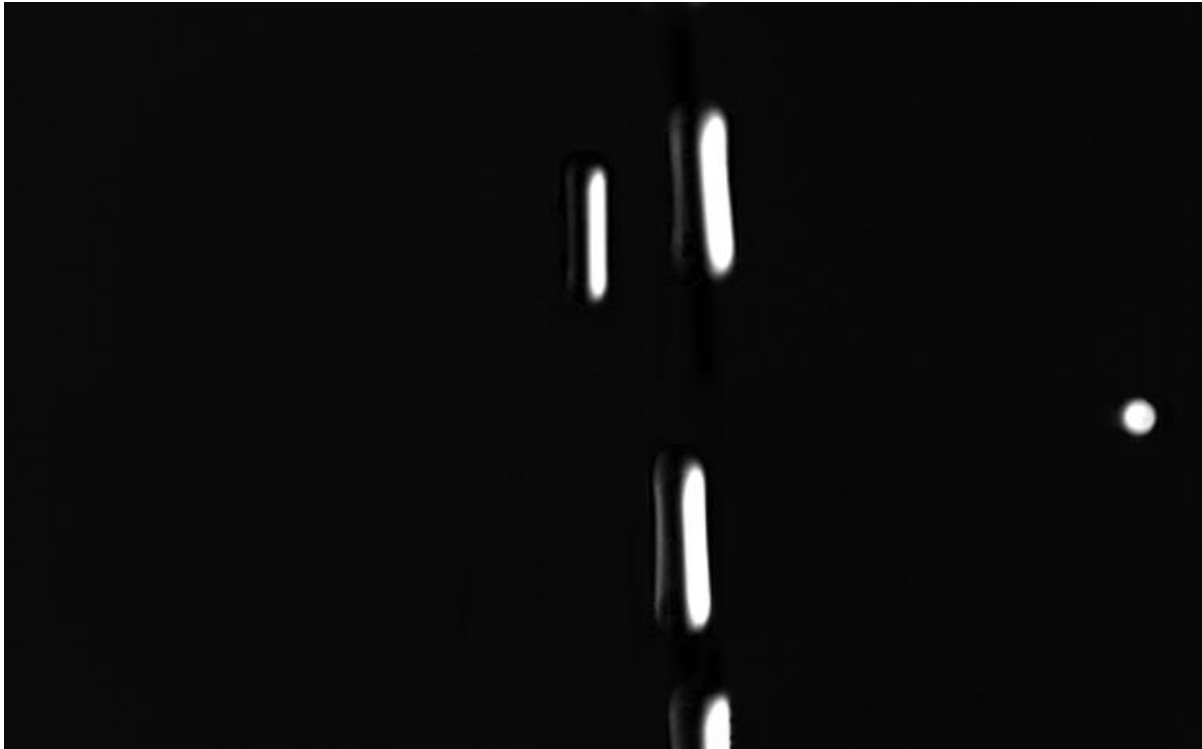


Figure 4.7 : The enhanced flow Image

High speed bubbly flow image with low brightness must be advanced to elevate represent of the bubble details. First, the histogram equalization is utilized to improve image illumination. Then the contrast of image is improved by nonlinear γ -regulation mapping, in which the gray level of image is plotted to the range from 0 to 1, and the low gray level is condensed by the $\gamma=0.3$. The enhanced image is treated by the smoothing technology subsequently (Fig. 4.7).



Figure 4.8 : The morphological filled cavity bubble shape

Although the cavity flow image is improved enough to reveal the shapes of bubbles, there are also noisy areas and non-cohesive boundary caused by the enhancement process. This leads to the cavity bubble recognition and image segmentation very difficult. To acquire continues boundary and enhance the quality of segmentation, morphology filtering is performed to eliminate the remaining noise and unfilled boundaries of the edge detecting. In theory, circular operator is much better for obtaining a smooth target boundary. But when the filtering operator is more than 4×4 , the objects end up with large deformation in this research. Consequently, a four zero corner 4×4 operator is utilized to apply morphologically filtering with twice *erosion* and *dilation*. Fig. 4.8 presents the results of morphological filtering. In order to evaluate the applied image processing, the original and resultant images are combined together in the Fig. 4.10. It is obvious that the two images agree very well, and the deformation of bubble during high speed flow is revealed clearly.

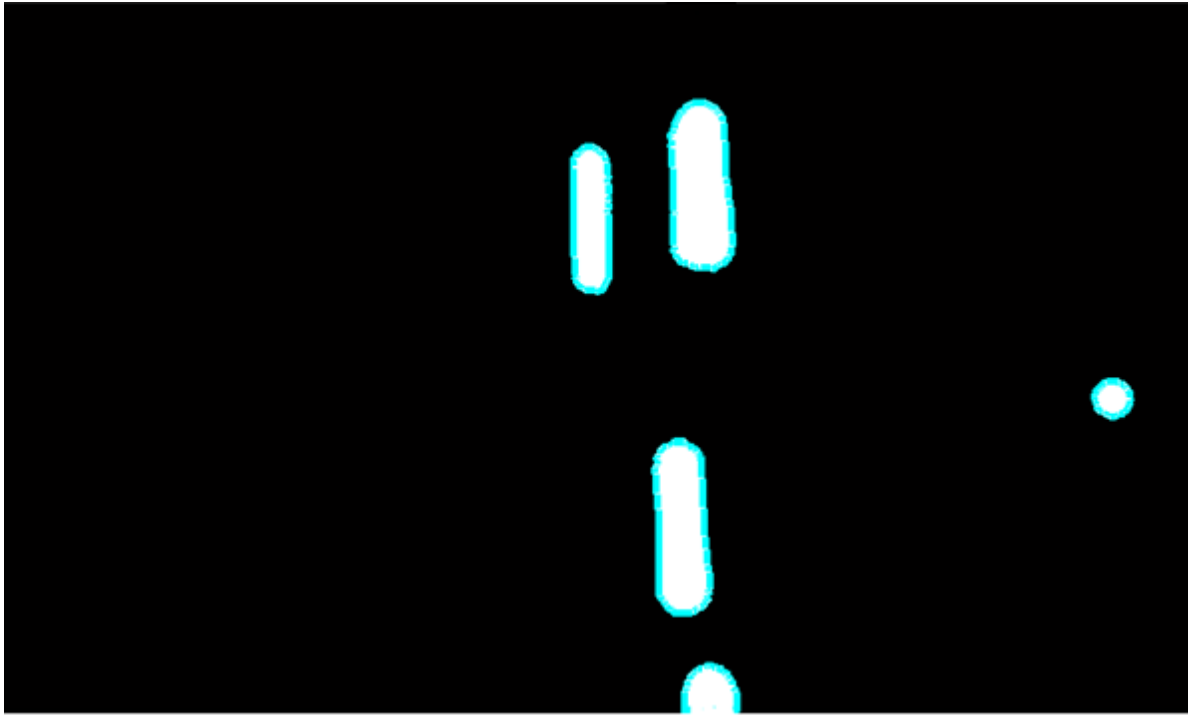


Figure 4.9 : The recognized edges of cavity bubbles

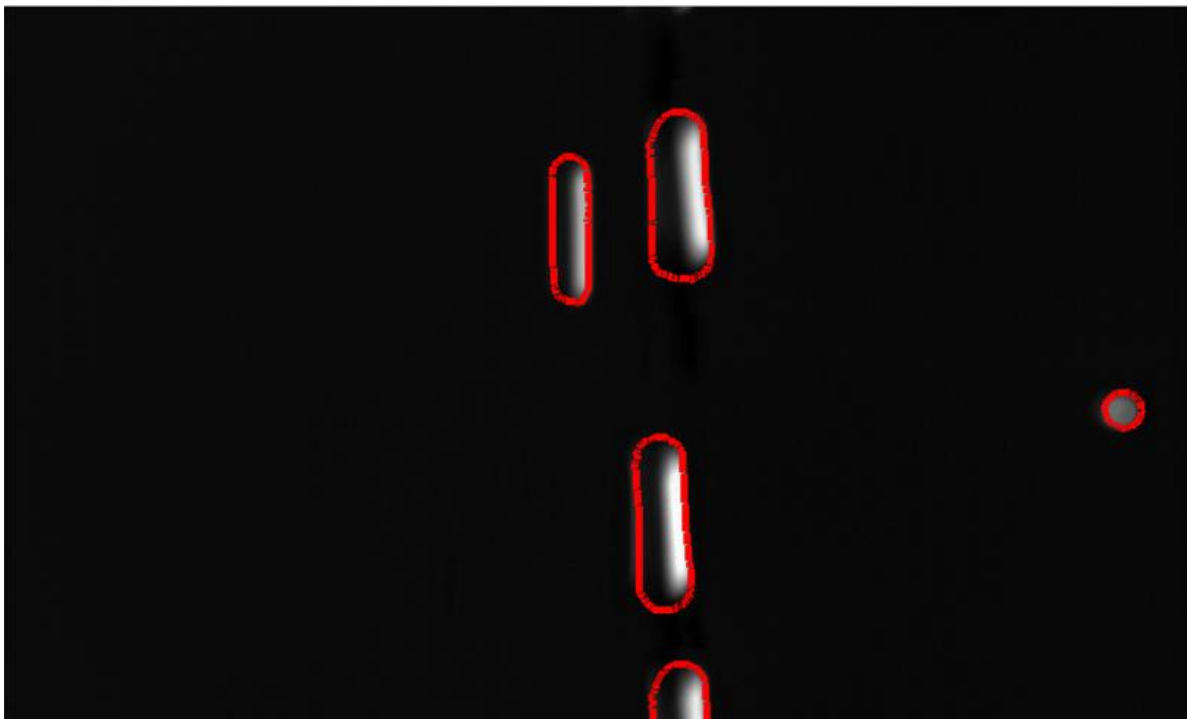


Figure 4.10 : Results of the processing operations of high speed cavity bubbles micro-flow images

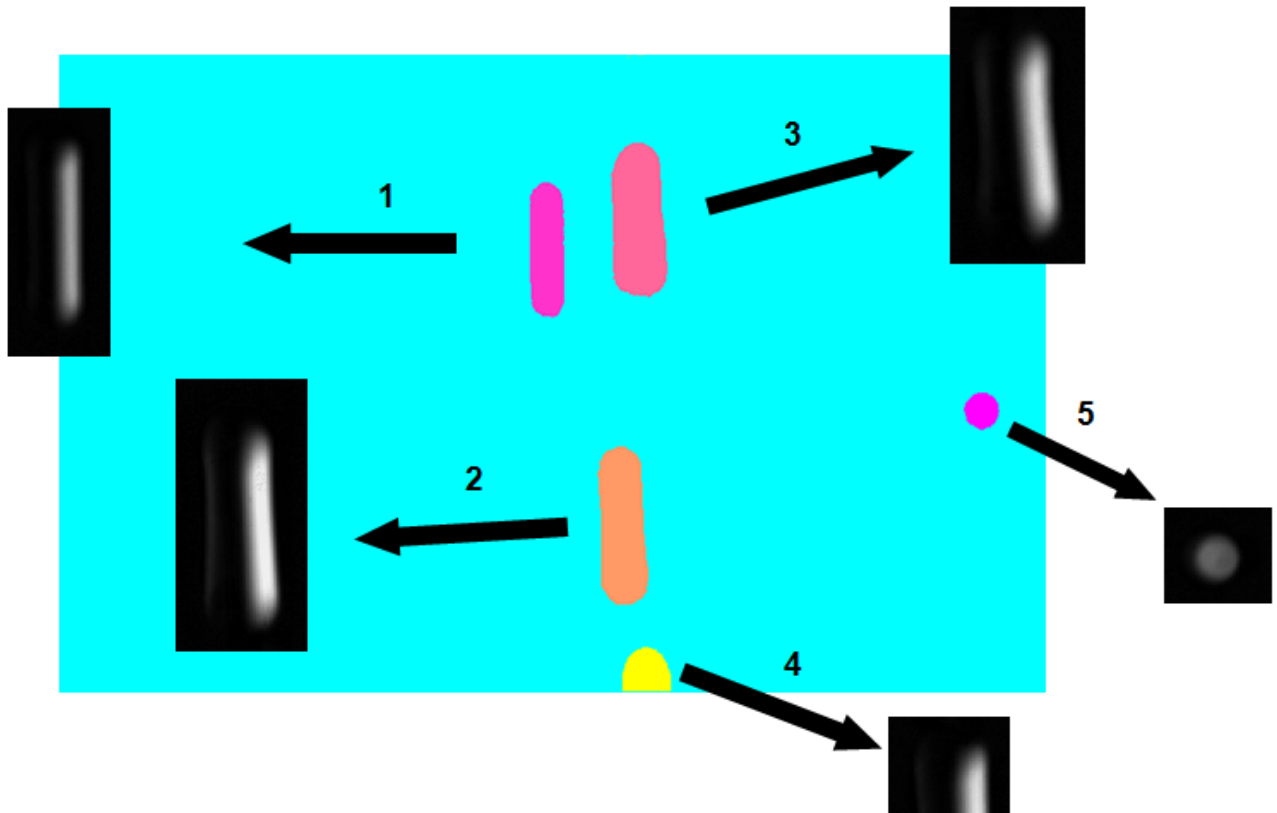


Figure 4.11 : Pseudo-colour indexed image

| <i>Bubbles</i> | <i>Area (Unit pixel)</i> | <i>Area (mm²)</i> | <i>Major Axis (mm)</i> | <i>Minor Axis (mm)</i> | <i>Eccentricity</i> |
|----------------|--------------------------|------------------------------|------------------------|------------------------|---------------------|
| 1 | 2819 | 0.0211 | 0.343 | 0.077 | 0.96 |
| 2 | 4338 | 0.0325 | 0.408 | 0.102 | 0.95 |
| 3 | 4809 | 0.036 | 0.391 | 0.123 | 0.93 |
| 4 | 1180 | 0.0088 | 0.128 | 0.091 | 0.52 |
| 5 | 648 | 0.0048 | 0.087 | 0.071 | 0.19 |

Table 4.1 : Detection and classification of individual bubbles

Results of direct recognition include area (calculated both in unit pixel and metric size), major axis, minor axis, and eccentricity. These parameters describe the flow status of each bubble in the microflow field. The metric calculation of bubble geometries are performed

using the real calibration parameters of the experimental setup consisting high speed CMOS camera and long distance microscope.

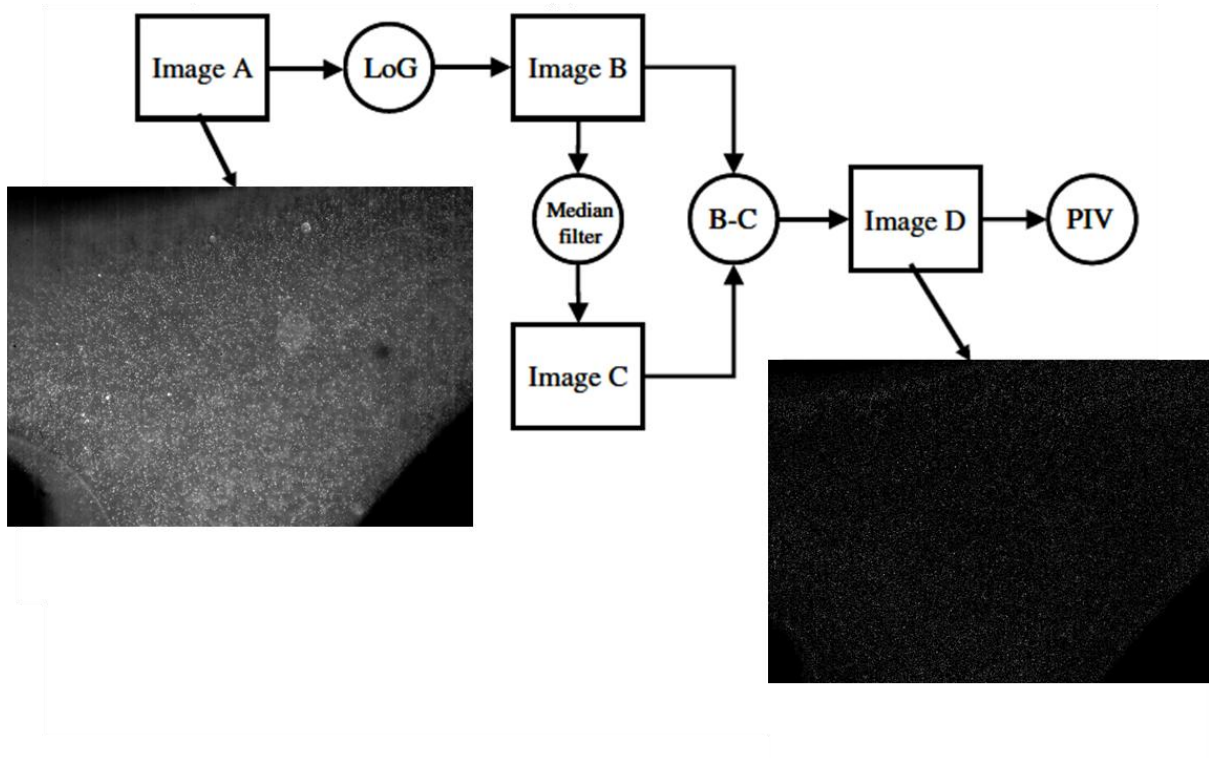


Figure 4.12 : Schematic diagram of the filter operations for phase discrimination by extracting the images of tracer particles from the pictures of the Hydrodynamic cavitation flow

The velocities of the continuous phase are determined by the application of particle image velocimetry (PIV) to the extracted images of the tracer particles. This extraction process, illustrated in Fig. 4.12, starts with an edge filter, which is called Laplacian of Gaussian (LoG). The fundamental characteristics of the LoG edge detector are the combination of a smoothing Gaussian filter and an enhancement step which is a Laplacian second derivative in two dimensions. The results of this procedure are revealed in Fig. 4.13.

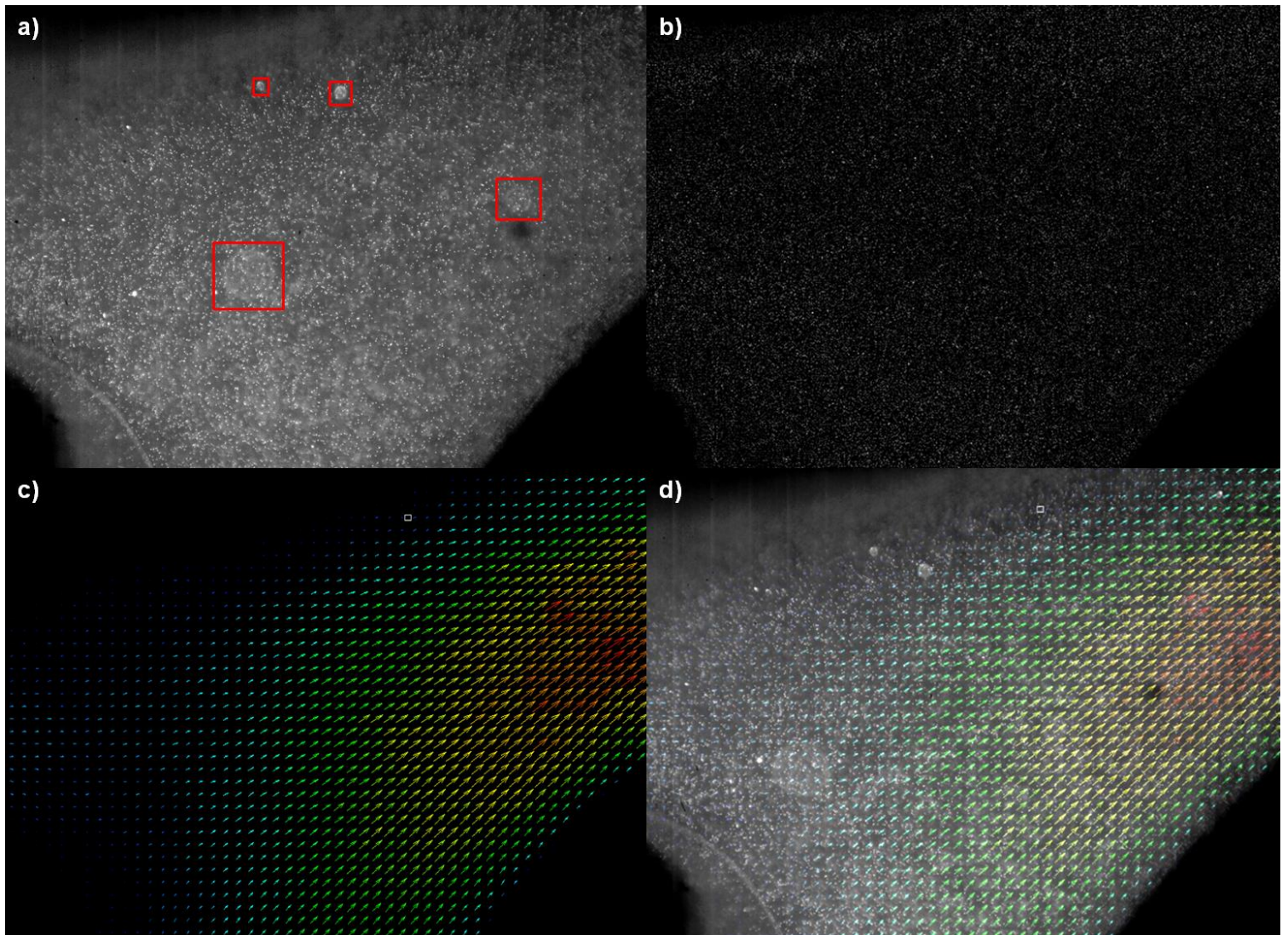


Figure 4.13 : (a) Original μ PIV Image (b) Filtered only tracer partial Image (c) Velocity vector map of the hydrodynamic cavitation (d) Instantaneous flow field of the continuous phase in the bubble column overlapped onto the original image containing bubbles and tracer. Mean velocities of the vector field have been subtracted to visualize the fluctuations (the colours of the vectors indicate the fluid velocity magnitude. Red: high velocity, blue: low velocity)

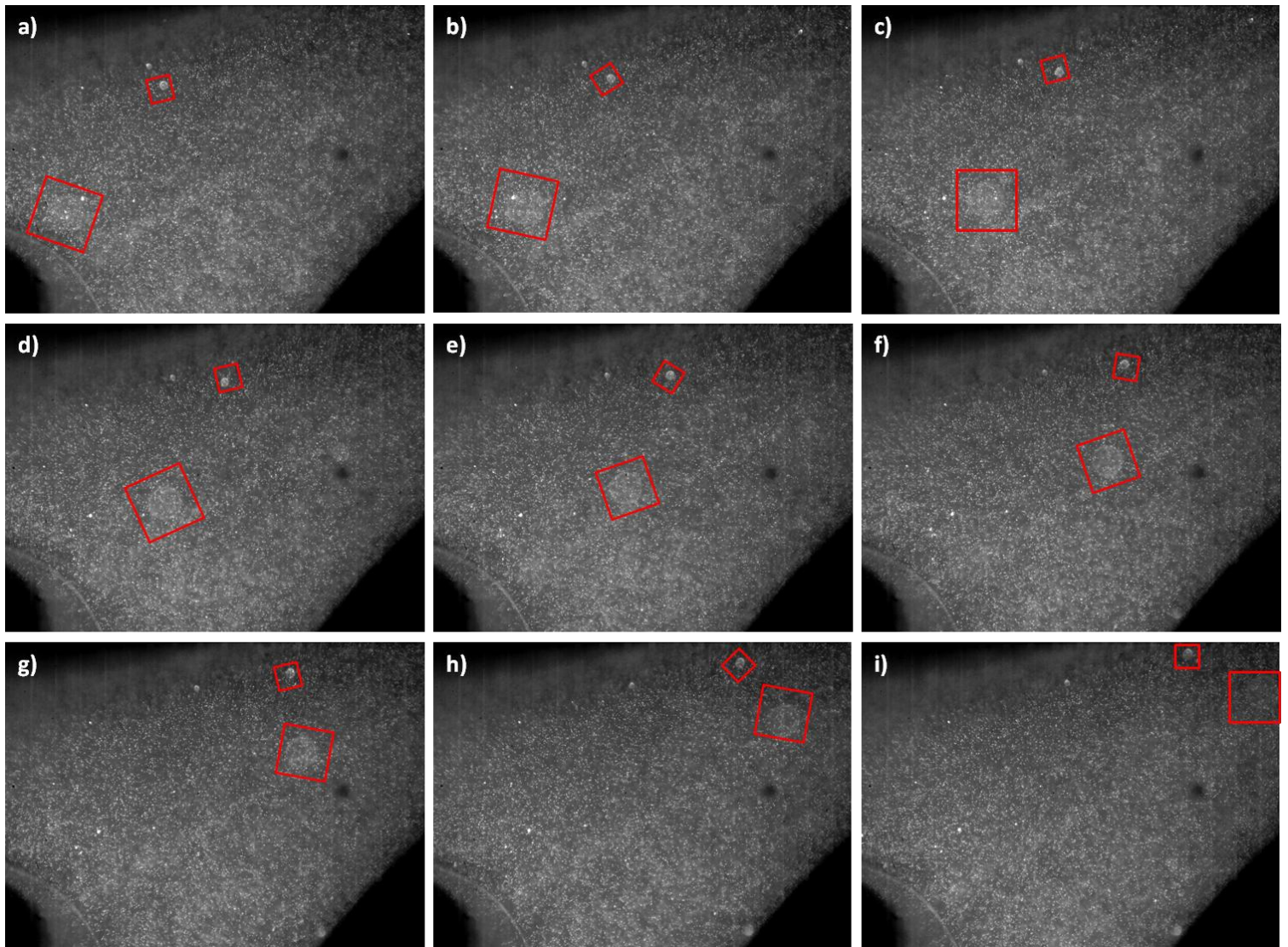


Figure 4.14 : Cavity bubbles tracking results of the ISPF algorithm

Tracking results of the μ PIV images are revealed in Fig. 4.14. The bubbles are mostly travel through the sides of the microchannel.

Chapter V

5 Conclusion and Future Work

For the visualization and analysis of hydrodynamic high-speed cavity bubbles, a measurement setup was improved which combines planar high resolution imaging using only background illumination and PIV procedures. The imaging plane for the bubbles was created using a long distance microscope with a very small depth of field and special filter operations in the image processing in order to remove out-of-focus objects (i.e. blurred bubbles and tracer particles). Therefore, it was possible to compute liquid and bubble velocity fields as well as bubble size, shape and orientation. The recognition of the bubble contour was based on using an edge detecting filter, which is much more robust than threshold methods performed to the grey scale of the images. Algorithms were implemented in Microsoft Visual C++ and OpenCV 2.4.2. Both metric and unit pixel size area-equivalent bubble diameter from planar images was evaluated. The bubble velocity field was determined by applying a tracking algorithm.

The continuous phase velocity field was determined by seeding the hydrodynamic cavitating flow with narrow-sized fluorescent particles and performing an edge detecting LoG filter in order to remove only sharply illustrated tracer images positioned within the imaging plane. In order to enable on-line evaluation of the double images with reasonable speed, Dynamic Studio Software, written by Dantec Dynamics A/S, is utilized to conduct measurement operations. With the identified PIV approach, instantaneous velocity fields within a bubble cloud as well as average velocity fields could be clarified by averaging 1000 double images.

In order to capture high data images, experiments were conducted in different flow pressures for the analysis of the hydrodynamic cavity bubbles in a special Lab-on-a-Chip. In that Lab-on-a-Chip, the interaction of two bubble streams in a mixing channel was analysed and the velocity fields of bubble and liquid phases were measured. Moreover, the experiments in both facilities showed that the bubble geometry mostly becomes ellipsoid when the bubble speed increases (by the effect of increasing pressure). Thus, the eccentricity as a function of the bubble size increases.

Furthermore, the effects of changing inlet pressure and changing probe-to-specimen distance are filtered out. Experiments showed that the probe-to-specimen distance is an important parameter to be optimized, since the maximum erosion rate was not achieved neither at the highest (7.75 mm) nor the lowest distance (0.5 mm), but at an optimum distance of 2.75 mm. A correlation to predict the erosion rate using probe-to-specimen distance, system parameters and material properties as variables was developed, which could predict the experimental results with a mean absolute error of 6.09%.

It was demonstrated that the developed planar imaging setup is a powerful method which yields reasonably good results on the visualization of hydrodynamic cavity bubbles as well as detailed information on bubble behaviour and their properties (i.e. microstructure of bubbles). The collected detailed data will be very useful for further improving the modelling of hydrodynamic bubbly cavitation that is used in kidney stone treatment.

References

- [1] Gravesen P, Branebjerg J, Jensen OS (1993) Microfluidics—a review. *J Micromech Microeng* 3:168–182
- [2] Stone HA, Stroock AD, Ajdari A (2004) Engineering flows in small devices: microfluidics toward a lab-on-a-chip. *Annu Rev Fluid Mech* 36:381–411
- [3] Yoshida H (2005) The wide variety of possible applications of micro-thermofluid controls. *Microfluid Nanofluid* 1:289–300. doi: 10.1007/s10404-004-0014-7
- [4] Lee SJ, Kim S (2009) Advanced particle-based velocimetry techniques for microscale flows. *Microfluid Nanofluid* 6:577–588. doi: 10.1007/s10404-009-0409-6
- [5] Cierpka C, Rossi M, Segura R, Kähler CJ (2011) On the calibration of astigmatism particle tracking velocimetry for microflows. *Meas Sci Technol* 22:015401. doi: 10.1088/0957-0233/22/1/015401
- [6] Santiago JG, Wereley ST, Meinhart CD, Beebe DJ, Adrian RJ (1998) A particle image velocimetry system for microfluidics. *Exp Fluids* 25(4):316–319
- [7] Bitsch L, Olesen LH, Westergaard CH, Bruus H, Klank H, Kutter JP (2005) Micro particle-image velocimetry of bead suspensions and blood flows. *Exp Fluids* 39(3):507–513
- [8] Singh AK, Cummings EB, Throckmorton DJ (2001) Fluorescent liposome flow markers for microscale particle-image velocimetry. *Anal Chem Columbus* 73(5):1057–1061
- [9] S. M. Hagsäter, C. H. Westergaard, H. Bruus, J. P. Kutter (2007) Investigations on LED illumination for micro-PIV including a novel front-lit configuration. *Exp Fluids* (2008) 44:211–219
- [10] Tassin A L and Nikitopoulos D E 1995 Non-intrusive measurements of bubble size and velocity *Exp. Fluids* 19 121–32
- [11] Borchers O, Busch C and Eigenberger G 1999 Analyse der Hydrodynamik in Blasenströmungen mit einer Bildverarbeitungsmethode *Proc. 2nd Workshop on Measurement Techniques for Steady and Transient Multiphase Flows, Rossendorf (Dresden), Germany*
- [12] Delnoij E, Westerweel J, Deen N G, Kuipers J A M and van Swaaij W P M 1999 Ensemble correlation PIV applied to bubble plumes rising in a bubble column *Chem. Eng. Sci.* 54 5159–71
- [13] Brücker Ch 2000 A detailed study of the role of the wake on the motion of single bubbles and bubble pairs using an advanced PIV-method *Proc. 9th Workshop on Two-*

- Phase Flow Predictions (Merseburg, Germany, 13–16 April 1999)* ed M Sommerfeld (Germany: Martin-Luther-Universität Halle-Wittenberg) pp 253–65
- [14] Deen N G, Hjertager B H and Solberg T 2000 Comparison of PIV and LDA measurement methods applied to the gas-liquid flow in a bubble column *10th Int. Symp. Application of Laser Techniques to Fluid Mechanics (Lisbon, Portugal)*
- [15] Lindken R, Meyer P and Merzkirch W 2000 Time resolved PIV measurements with systems of bubbles rising in water *Proc. ASME Fluids Engineering Division Summer Meeting (Boston, MA, USA)* Paper FEDSM2000–11200
- [16] Fujiwara A, Takahashi T, Tokuhiko A and Hishida K 2001 Turbulent microscale structure in bubbly channel flow *Int. Conf. On Multiphase Flow (New Orleans, USA)*
- [17] Hassan Y A, Ortiz-Villafuerte J and Schmidl W D 2001 Three-dimensional measurements of single bubble dynamics in a small diameter pipe using stereoscopic particle image velocimetry *Int. J. Multiphase Flow* 27 817–42
- [18] Bröder D and Sommerfeld M 2001 Experimental studies of the hydrodynamics in a bubble column by an imaging PIV/PTV-system *Proc. 4th Int. Symp. on Particle Image Velocimetry (Göttingen, Germany)*
- [19] Bröder D and Sommerfeld M 2002 An advanced LIF-PLV system for analysing the hydrodynamics in a laboratory bubble column at higher void fraction *Exp. Fluids* 33 826–37
- [20] Bröder D and Sommerfeld M 2007 Planar shadow image velocimetry for the analysis of the hydrodynamics in bubbly flows *Meas. Sci. Technol.* 18 (2007) 2513–2528
- [21] Honkanen M, Saarenrinne P, Stoor T and Niinimäki J 2005 Recognition of highly overlapping ellipse-like bubble images *Meas. Sci. Technol.* 16 1760–70
- [22] Bilen, H., Unel, M., 2008, “*Micromanipulation Using a Microassembly Workstation with Vision and Force Sensing*”, Lecture Notes in Computer Science, 5226, pp. 1164-1172.
- [23] Bilen, H., Hocaoglu, M. A., Baran, E., Unel, M., Gozuacik, D., 2009, “*Novel Parameter Estimation Schemes in Microsystems*”, Proceedings of IEEE International Conference on Robotics and Automation (ICRA’09), pp. 2394-2399.
- [24] Bilen, H., Hocaoglu, M., Unel, M., Sabanovic, A., 2012, “*Developing Robust Vision Modules for Microsystems Applications*”, Machine Vision and Applications, 23 (1), pp. 25–42.

- [25] Kosar, A., Sesen, M., Oral, O., Itah, Z., Gozuacik, D., 2011, "*Bubbly Cavitating Flow Generation and Investigation of Its Erosional Nature for Biomedical Applications*", IEEE Transactions on Biomedical Engineering, 58 (5), pp. 1337-1346.
- [26] Itah, Z., Oral, O., Sesen, M., Perk, O. Y., Erbil, S., Demir, E., Ekici, I. D., Ekici, S., Kosar, A., Gozuacik, D., 2013, "*Hydrodynamic Cavitation Kills Prostate Cells and Ablates Benign Prostatic Hyperplasia Tissue*", Experimental Biology and Medicine, 238 (11), pp. 1242-1250.
- [27] Perk, O. Y., Sesen, M., Gozuacik, D., Kosar, A., 2012, "*Kidney Stone Erosion by Hydrodynamic Cavitation and Consequent Kidney Stone Treatment*", Annals of Biomedical Engineering, 40, pp. 1895-1902.
- [28] Palanker D, Vankov A, Miller J, Friedman M, Strauss M (2003) Prevention of Tissue Damage by Water Jet During Cavitation. J Appl Phys 94:2654–2661.
- [29] An Y 2011 Phys. Rev. E 84 066313
- [30] Yasui K, Iida Y, Tuziuti T, Kozuka T and Towata A 2008 Phys. Rev. E 77 016609
- [31] An Y 2012 Phys. Rev. E 85 016305
- [32] Yasui K, Towata A, Tuziuti T, Kozuka T and Kato K 2011 J. Acoust. Soc. Am. 130 3233.
- [33] Toytman I, Silbergleit A, Simanovski D and Palanker D 2010 Phys. Rev. E 82 046313.
- [34] I. Lavon, J. Kost, 'Ultrasound and transdermal drug delivery', Drug Discovery Today, 9, 2004, 670–676.
- [35] J. P. Whelan and B. Finlayson, 'An experimental model for the systematic investigation of stone fracture by extracorporeal shock wave lithotripsy', J. Urol., 140, 1988, 395–400.
- [36] C. Chaussy, E. Schmiedt, D. Jocham, V. Walther, W. Brendel, B. Forssmann, and W. Hepp, 'Extracorporeal Shock Wave Lithotripsy: New Aspects in the Treatment of Kidney Stone Disease', Basel, Switzerland, Karger, 1982.
- [37] M. Delius, G. Heine, W. Brendel, 'A mechanism of gallstone destruction by extracorporeal shock waves', Naturwiss., 75, no. 4, 1988, 200–201.
- [38] S. R. Khan, R. L. Hackett, and B. Finlayson, 'Morphology of urinary stone particles resulting from ESWL Treatment', J. Urol., 136, 1986, 1367–1372.
- [39] W. Sass, M. Braunlich, H-P. Dreyer, E. Matura, W. Forberth, H-G. Priesmeyer, J. Seifert, 'The mechanisms of stone disintegration by shock waves', Ultrasound. Med. Biol., 17, 1991, 239–243.

- [40] N.G. Holmer, L.O. Almquist, T.G. Hertz, A. Holm, E. Lindstedt, H.W. Persson, C.H. Hertz, 'On the mechanism of kidney stone disintegration by acoustic shock waves', *Ultra. Med. Biol.*, 17, 1991, 479–489.
- [41] Prinz C, Lindner O, Bitter T, et al: Extracorporeal cardiac shock wave therapy ameliorates clinical symptoms and improves regional myocardial blood flow in a patient with severe coronary artery disease and refractory angina. *Case Report Med* 2009, 2009:639594
- [42] Smith, N., Zhong, P., 'Stone comminution correlates with the average peak pressure incident on a stone during shock wave lithotripsy', *JOURNAL OF BIOMECHANICS*, 2520-2525, 45, 2012.
- [43] Adrian RJ (1991) Particle imaging techniques for experimental fluid mechanics. *Annu Rev Fluid Mech* 23:261–304
- [44] Raffel, M., Willert, C. E., Wereley, S. T., Kompenhans, J. (2007) "Particle Image Velocimetry-A Practical Guide" Springer-Verlag.
- [45] Samimy M., Wernet M. P. (2000) "Review of planar multiple-component velocimetry in high speed flows" *AIAA Journal*, 38, pp. 553–574.
- [46] Rafael C. Gonzalez, Richard E. Woods, "Digital Image Processing", 2nd ed., Beijing: Publishing House of Electronics Industry, 2007
- [47] S.Aksoy, "Image Segmentation", Department of Computer Engineering, Bilkent Univ.
- [48] K. G. Gunturk, "EE 7730- Image Analysis I", Louisiana state university.
- [49] W. X. Kang, Q. Q. Yang, R. R. Liang, "The Comparative Research on Image Segmentation Algorithms", *IEEE Conference on ETCS*, pp. 703-707, 2009.
- [50] N. R. Pal, S. K. Pal, "A Review on Image Segmentation Techniques", *Pattern Recognition*, Vol. 26, No. 9, pp. 1277-1294, 1993
- [51] H. Zhang, J. E. Fritts, S. A. Goldman, "Image Segmentation Evaluation: A Survey of unsupervised methods", *computer vision and image understanding*, pp. 260-280, 2008.
- [52] K. K. Singh, A. Singh, "A Study of Image Segmentation Algorithms for Different Types of Images", *International Journal of Computer Science Issues*, Vol. 7, Issue 5, 2010.
- [53] S. S. Varshney, N. Rajpal, R. Purwar, "Comparative Study of Image Segmentation Techniques and Object Matching using Segmentation", *Proceeding of International Conference on Methods and Models in Computer Science*, pp. 1-6, 2009.
- [54] P. Karch, I. Zolotova, "An Experimental Comparison of Modern Methods of Segmentation", *IEEE 8th International Symposium on SAMI*, pp. 247-252, 2010.

- [55] H. G. Kaganami, Z. Beij, "Region Based Detection versus Edge Detection", IEEE Transactions on Intelligent information hiding and multimedia signal processing, pp. 1217-1221, 2009.
- [56] L.Aurdal, "Image Segmentation beyond thresholding", Norsk Regnesentral, 2006.
- [57] Y. Zhang, H. Qu, Y. Wang, "Adaptive Image Segmentation Based on Fast Thresholding and Image Merging", Artificial reality and Telexistence-Workshops, pp. 308-311, 1994.
- [58] X. Jiang, R. Zhang, S. Nie, "Image Segmentation Based on PDEs Model: a Survey", IEEE conference, pp. 1-4, 2009.
- [59] Gonzalez, R.C., Woods, R.E. and Eddins, S.L., Digital Image Processing, Prentice Hall, New Jersey, 366-374 (2004).
- [60] H. Wang, D. Suter, K. Schindler, and C. Shen, "Adaptive object tracking based on an effective appearance filter," *IEEE Trans. Pattern Anal. Mach. Intell.*, vol. 29, no. 9, pp. 1661–1667, Sep. 2007.
- [61] F. Porikli, O. Tuzel, and P. Meer, "Covariance tracking using model update based on lie algebra," in *Proc. IEEE CVPR*, 2006, pp. 728–735.
- [62] M. Piccardi and E. Cheng, "Multi-frame moving object track matching based on an incremental major color spectrum histogram matching algorithm," in *Proc. IEEE CVPR*, 2005, p. 19.
- [63] E.K.-M. K. Nummiaro and L. Gool, "An adaptive color-based particle filter," *Image Vis. Comput.*, vol. 21, no. 1, pp. 99–110, 2003.
- [64] Zhang, W. Hu, S. Maybank, and X. Li, "Graph based discriminative learning for robust and efficient object tracking," in *Proc. ICCV*, 2007, pp. 1–8.
- [65] M. Isard and A. Blake, "Condensation: Conditional density propagation for visual tracking," *Int. J. Comput. Vis.*, vol. 29, no. 1, pp. 5–28, 1998.
- [66] B. Babenko, M. Yang, and S. Belongie, "Visual tracking with online multiple instance learning," in *Proc. IEEE CVPR*, 2009, pp. 983–990.
- [67] K. Zimmermann, J. Matas, and T. Svoboda, "Tracking by an optimal sequence of linear predictors," *IEEE Trans. Pattern Anal. Mach. Intell.*, vol. 31, no. 4, pp. 677–692, Apr. 2009.
- [68] X. Zhang, W. Hu, S. Maybank, X. Li, and M. Zhu, "Sequential particle swarm optimization for visual tracking," in *Proc. IEEE CVPR*, 2008, pp. 1–8.
- [69] Duineveld P C 1994 Bouncing and coalescence of two bubbles in water *PhD Thesis* University of Twente, The Netherlands ISBN 90–9007541-0.

- [70] M. Li, T. Tan, W. Chen, and K. Huang, "Efficient object tracking by incremental self-tuning particle filtering on the affine group," *IEEE Trans. On Image Processing*, vol. 21, no. 3, March 2012.
- [71] Crowe, C. T., 2006, "*Multiphase Flow Handbook*", Boca Raton, FL: CRC Press.
- [72] Dantec Dynamics A/S, 2006.
- [73] Rajeshwar Dass, Priyanka, Swapna Devi, "*Image Segmentation Techniques*", *IJECT*, Vol. 3, Issue 1, 2012.